

Chapter 3

Bolocam Survey for 1.1 mm Dust Continuum Emission in the Ophiuchus Molecular Cloud

Abstract

We present a large-scale millimeter continuum map of the Ophiuchus molecular cloud. Nearly 11 square degrees, including all of the area in the cloud with $A_V \geq 3$ magnitudes, was mapped at 1.1 mm with Bolocam on the Caltech Submillimeter Observatory (CSO). By design, the map also covers the region mapped in the infrared with the *Spitzer Space Telescope*. We detect 44 definite sources, and a few likely sources are also seen along a filament in the eastern streamer. The map indicates that dense cores in Ophiuchus are very clustered and often found in filaments within the cloud. Most sources are round, as measured at the half power point, but elongated when measured at lower contour levels, suggesting spherical sources lying within filaments. The masses, for an assumed dust temperature of 10 K, range from 0.24 to 3.9 M_\odot , with a mean value of 0.96 M_\odot . The total mass in distinct cores is 42 M_\odot , 0.5% to 2% of the total cloud mass, and the 1.1 mm mass above 4σ is about 80 M_\odot . The mean densities of the cores are quite high, with an average of $1.6 \times 10^6 \text{ cm}^{-3}$, suggesting short free-fall times. The core mass distribution can be fitted with a power law with slope $\alpha = 2.1 \pm 0.3$ for $M > 0.5 M_\odot$, similar to that found in other regions, but

Portions of this chapter were previously published in Young, Enoch, Evans, et al. 2006, ApJ, 644, 326.

slightly shallower than that of some determinations of the local IMF. In agreement with previous studies, our survey shows that dense cores account for a very small fraction of the cloud volume and total mass. They are nearly all confined to regions with $A_V \geq 11$ mag, a lower threshold than found previously.

3.1 Introduction

The Ophiuchus molecular cloud is a well-known birthplace of stars. Located at a distance of 125 ± 25 pc (de Geus, de Zeeuw, & Lub, 1989), Ophiuchus contains the L1688 dark cloud region, which contains the Ophiuchus cluster ($16^h 27^m, -24^\circ 30'$ (J2000)) of young stars and embedded objects. The cluster region has been studied in great detail at a variety of wavelengths from millimeter molecular lines (Loren 1989; Ridge et al. 2006) to near-infrared (e.g., Wilking, Lada, & Young 1989; Allen et al. 2002) to X-ray (Imanishi, Koyama, & Tsuboi, 2001). It has also been mapped in dust continuum emission (Johnstone et al. 2000; Motte, André, & Neri 1998). The embedded cluster is itself surrounded by a somewhat older population of stars extending over 1.3 deg^2 (Wilking et al., 2005). The cloud is home to two other known regions of star formation, the Lynds dark clouds L1689 ($16^h 32^m, -24^\circ 29'$) and L1709 ($16^h 31^m, -24^\circ 03'$). However, little is known about star formation outside of these three regions.

In this chapter we present the first large-scale millimeter continuum map of the entire Ophiuchus molecular cloud. This survey represents the second in the series of millimeter surveys of three nearby molecular clouds: Perseus (Enoch et al. 2006; chapter 2), Ophiuchus, and Serpens (Enoch et al. 2007; chapter 4). Maps at millimeter wavelengths of the dust continuum emission find regions of dense gas and dust, both those with embedded protostars and those that are starless. Previously published maps of the Ophiuchus cloud covered only small regions: Motte et al. (1998) mapped about 0.13 deg^2 at 1.3 mm and Johnstone et al. (2000) mapped about 0.19 deg^2 at $850 \mu\text{m}$. A larger (4 deg^2) map at $850 \mu\text{m}$ is referred to but not published by Johnstone, Di

Francesco, & Kirk (2004); it is available from the COMPLETE website¹ and discussed in Ridge et al. (2006). Most recently, Stanke et al. (2006) have mapped a 1.3 deg² area of L1688 at 1.2 mm. Our map covers 10.8 deg², providing a total picture of the dense gas in Ophiuchus.

Our survey complements the *Spitzer* c2d Legacy project “From Molecular Cores to Planet-forming Disks” (Evans et al., 2003). All of the area in the cloud with $A_V \geq 3$ magnitudes (according to the map of Cambr esy (1999)) was observed with Bolocam and the InfraRed Array Camera (IRAC) on *Spitzer* (figure 3.1). A somewhat larger area was also mapped at 24, 70, and 160 μm with the Multiband Imaging Photometer for Spitzer (MIPS). Maps of millimeter molecular line emission for this same area have been made by the COMPLETE team² (Goodman 2004; Ridge et al. 2006). Previously, the largest maps of molecular lines were those of Loren (1989) and Tachihara, Mizuno, & Fukui (2000).

This chapter applies the analysis methods described in chapter 2. Observations with Bolocam (§3.2), data reduction (§3.3), and source identification (§3.3.3) are described to the extent that they differ from those detailed in chapter 2 for Perseus. Basic results including cloud morphology and source properties are presented in §3.4. Completeness is discussed in §3.5.1, the core mass distribution in §3.5.2, clustering of cores in §3.5.3, and an extinction threshold for finding cores in §3.5.4

3.2 Observations

We mapped the Ophiuchus molecular cloud at 1.12 mm (hereafter 1.1 mm for brevity) with Bolocam on the Caltech Submillimeter Observatory (CSO)³ during two observing runs: 21 May – 09 June 2003 and 06 – 11 May 2004. See chapter 2 for information about the instrument. In May 2003, there were 95 channels; in May 2004, the observations were taken with 114 channels. The cloud was observed in three large sections,

¹<http://cfa-www.harvard.edu/COMPLETE>

²<http://cfa-www.harvard.edu/COMPLETE>

³The CSO is operated by the California Institute of Technology under funding from the National Science Foundation, contract AST-0229008.

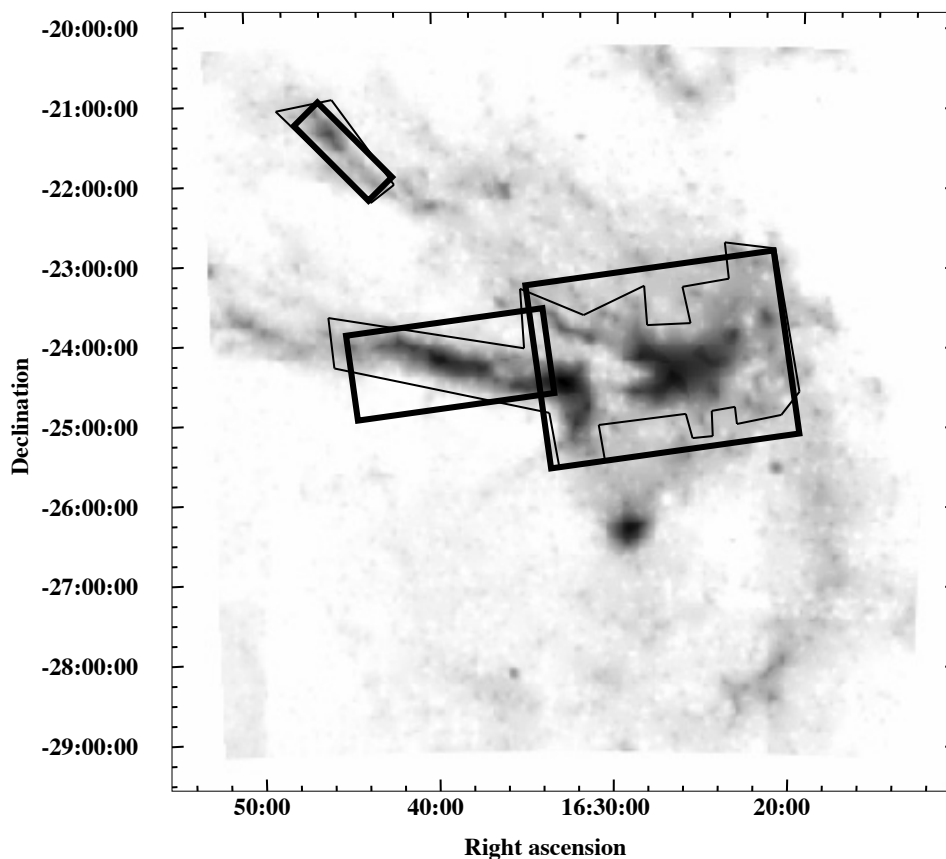


Figure 3.1 Extinction map of Ophiuchus from Cambr sy (1999) with the outline of the Bolocam observation area (thick lines) and the *Spitzer* IRAC observation area (thin lines). The area observed with IRAC was chosen to cover the cloud down to $A_V \geq 3$. The Bolocam observations were designed to cover approximately the same region observed with IRAC.

as indicated in figure 3.1: the main L1688 cluster region, the large eastern streamer that extends to the east of L1689, and a smaller northeastern streamer that is not contiguous with the other regions.

Each section was observed with a scan rate of $60''$ per second, with subsequent subscans offset from the previous one by $162''$, perpendicular to the scan direction. With this scan pattern, 1 deg^2 was observed with 23 subscans in approximately half an hour of telescope time, including 20-second turn-around times at the edges of the maps. Map sections were scanned in two orthogonal directions, rotated slightly from

right ascension (RA) and declination (Dec) by small angles. This technique allows for good cross-linking of the final map with sub-Nyquist sampling and minimal striping from $1/f$ noise. The northeastern streamer is a little more than 0.5 deg^2 , the eastern streamer section is about 2.7 deg^2 , and the large L1688/main cloud section covers a total of 7.4 deg^2 , which was observed in four sections of approximately 4 deg^2 each.

The best-weather observations from both runs for each of the three sections were averaged and combined into a single large map: for the northeastern streamer, three scans in RA and three in Dec, were combined for a total observation time of 4.4 hours. The eastern streamer sections consists of three scans in RA and two in Dec, contributing 6 hours of observation time. The main cloud region was observed in four pieces, with two RA and two Dec scans each, requiring 13 hours of integration time. The resulting coverage varies by $\sim 25\%$.

In addition to the Ophiuchus maps, small maps of secondary calibrators and pointing sources were made every 2 hours throughout the run. All observed calibration sources used to derive the flux calibration factor for that run. Planets provided beam maps and primary flux calibration sources. Uranus and Mars were observed during both runs, and Neptune was also observed on the May 2004 run.

3.3 Data Reduction

3.3.1 Pointing and Flux Calibration

A pointing model was generated from beam maps of planets, Galactic HII regions, and the protostellar source IRAS 16293–2422, which lies within the Ophiuchus cloud complex. For May 2003, the root-mean-square (rms) pointing uncertainty was $6''$, based on the dispersion of the centroid of IRAS 16293–2422 after the pointing model was applied. For May 2004, the rms pointing uncertainty was $2''$ to $3''$; however, the number of IRAS 16293–2422 observations is small (seven), so the rms is not well characterized.

A flux density calibration curve was generated for each run from observations of

planets and secondary calibrators (Sandell, 1994) throughout each night and over a range of elevations, thereby sampling a large range in atmospheric optical depths.

3.3.2 Iterative Mapping

The iterative mapping procedure described in §2.3.4 was run for each section of Ophiuchus and for each observing run. The May/June 2003 data and May 2004 were iteratively mapped separately because they required different calibration and pointing corrections. The final map is a weighted average of the maps from each run.

3.3.3 Source Identification

After the final calibrated maps were created, sources were identified as in §2.4.1. The average coverage in the map varies from 40 hits per pixel, or 20 sec of integration time, in most of the L1688 region, to 60 hits pixel⁻¹ (30 sec of integration) in the northeastern streamer. Only parts of the map with coverage greater than 0.22 times the maximum coverage (corresponding to a range in the local rms over the map of a factor of ~ 2), were used for source finding. Finally, a peak-finding routine was used to detect sources in the Wiener-filtered map above 4 times the local rms noise.

A detection limit as low as 4σ was necessary to detect some previously known sources from earlier SCUBA 850 μm surveys (Johnstone et al., 2000). This limit was not strict enough to avoid all false detections, however, and some artifacts were incorrectly identified as sources. Therefore, each source was also inspected by eye. Most of the artifacts were unambiguous because they were found close to the edges of the map or were caused by striping: one pixel wide and extended in one of the scan directions. Single-pixel peaks were also discarded, which might have excluded some faint sources. Although in principle it should be possible to recover structure up to the array size of $7.5'$, it was found in chapter 2 that structures larger than approximately $4'$ are severely affected by cleaning, and not well recovered by iterative mapping.

3.4 Results

3.4.1 General Cloud Morphology

The map of the cloud is shown in figure 3.2, with known regions identified. Our map covers 10.8 deg^2 (51.4 pc^2 at a distance of 125 pc), which is equivalent to 1.4×10^5 resolution elements given the beam size of $31''$. Most of the compact emission is confined to the L1688 cluster region. Several sources are also detected in L1709, L1689, and around the extensively studied Class 0 protostar IRAS 16293–2422. No emission that is extended $\gtrsim 2'$ is seen in the map.

The noise in the final map varied from section to section because of differences in the number of good observations and changes in sky noise. A map of the noise (figure 3.3) shows the variations in noise in the different map areas, ranging from 11 to 30 mJy beam $^{-1}$. The average rms in the regions of the map where most sources were detected was about 27 mJy beam $^{-1}$. High noise regions are apparent in figure 3.3 as a strip above L1709 and in the regions around strong sources, especially in the L1688 cluster.

We detected 44 sources with signal-to-noise greater than 4σ that were confirmed as real by inspection. Sources are listed in table 3.1 and identified as Bolo 1, etc. All sources were identified in the main cloud and eastern streamer sections. Figure 3.4 plots the positions of the sources as red circles on the grayscale 1.1 mm map, with insets showing magnifications of the densest source regions. We did not detect any sources in the northeastern streamer, where the noise is lowest. Most of the sources are concentrated in the previously well-studied regions in Ophiuchus, suggesting that dense cores are highly clustered in the Ophiuchus cloud. Figure 3.4 contains blowups of the main regions of emission, including the well known Ophiuchus cluster in L1688, L1689, IRAS 16293–2422, and L1709.

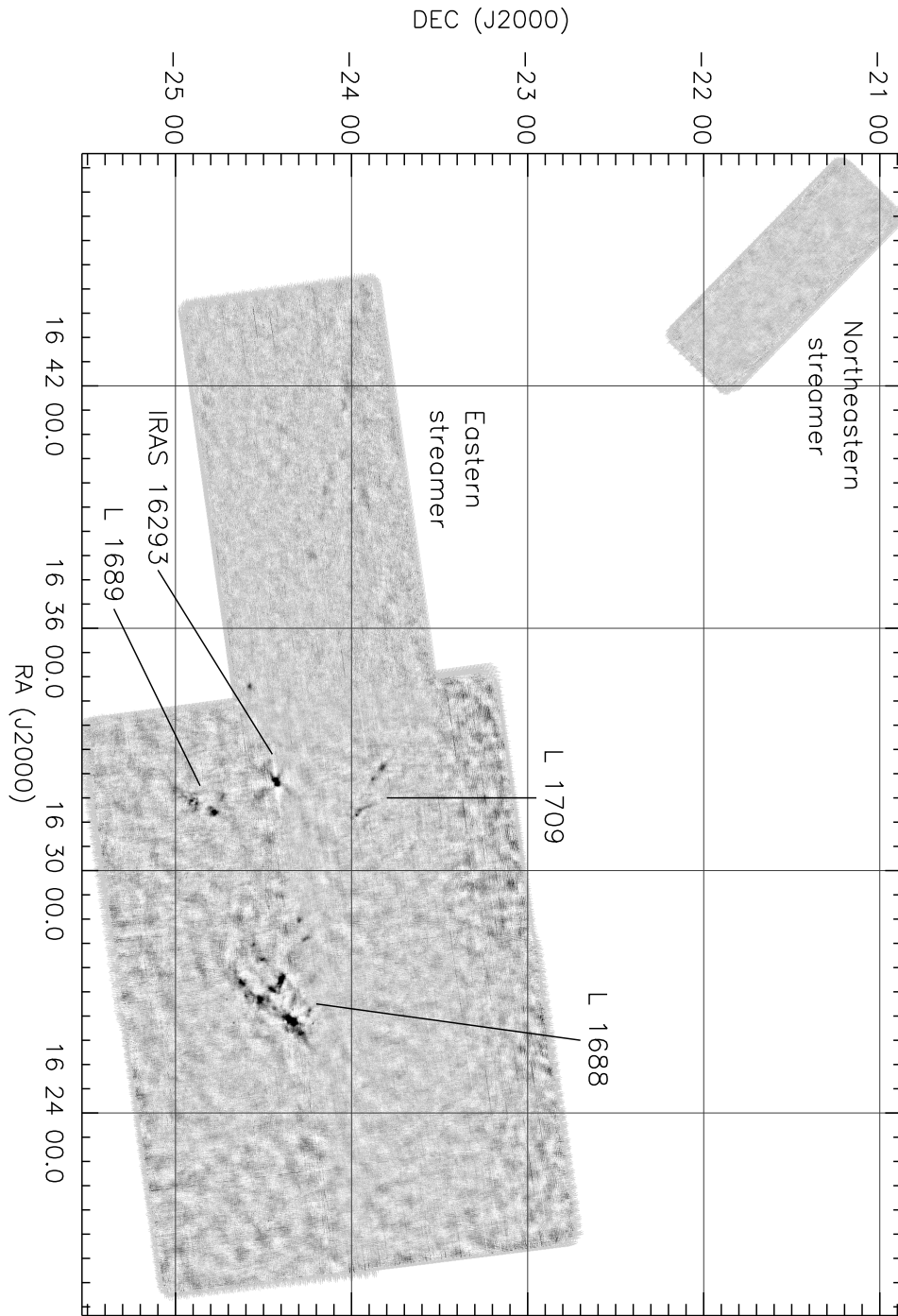


Figure 3.2 1.1 mm Bolocam map of 10.8 deg^2 (51.4 pc^2 at $d = 125 \text{ pc}$) in the Ophiuchus molecular cloud, with $10''$ pixels and a beam size of $31''$. The gray scale is proportional to intensity weighted by the coverage to avoid confusion by noise in regions with low coverage. Well-known regions and those discussed by name in the text are indicated.

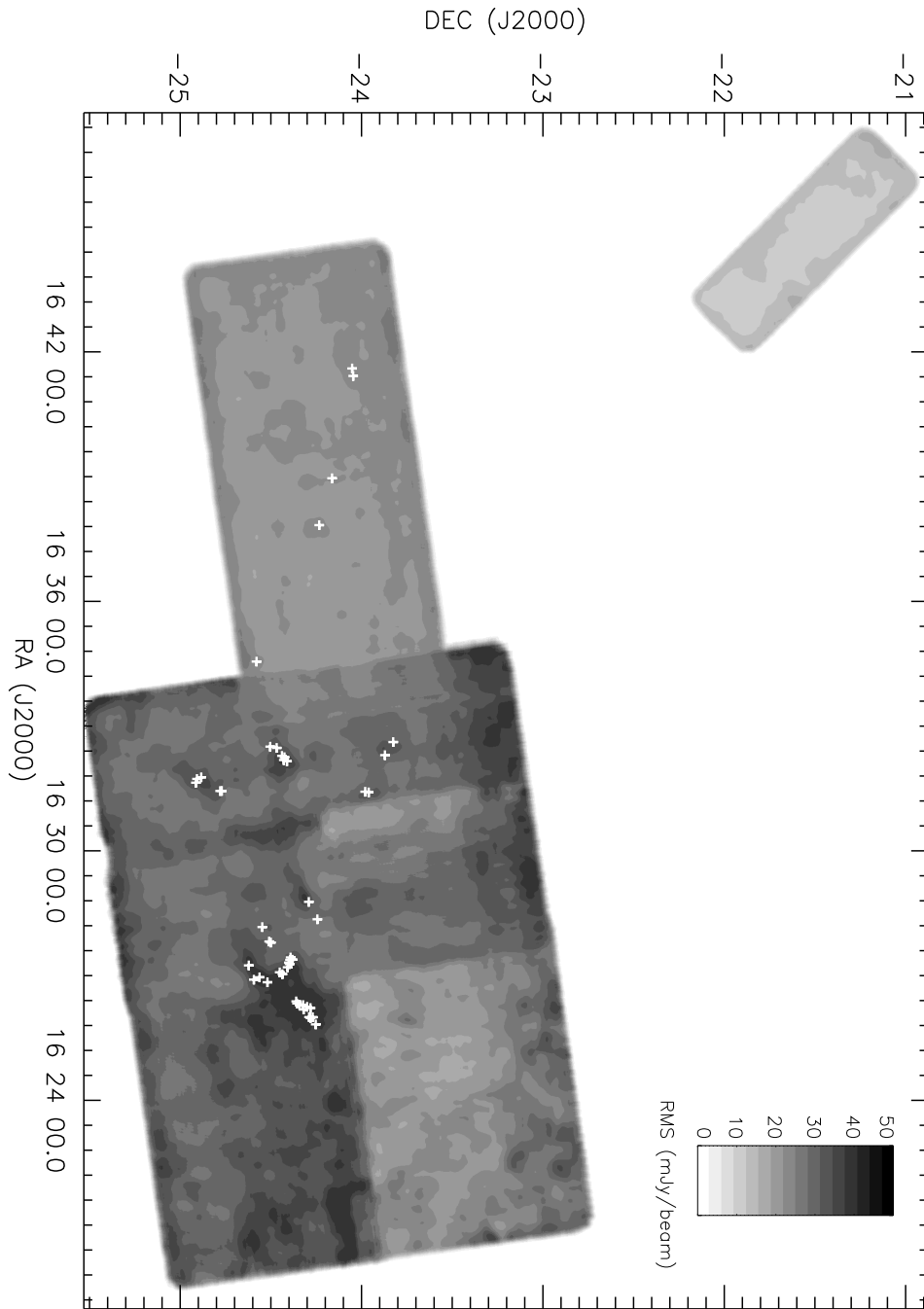


Figure 3.3 A map of the noise in gray scale with sources indicated by white plus signs. The gray scale runs from 11 mJy beam^{-1} to 30 mJy beam^{-1} . High noise regions are apparent in a strip above L1709, and in the area containing L1688. Note the increased noise near bright sources caused by residual systematics from sky subtraction.

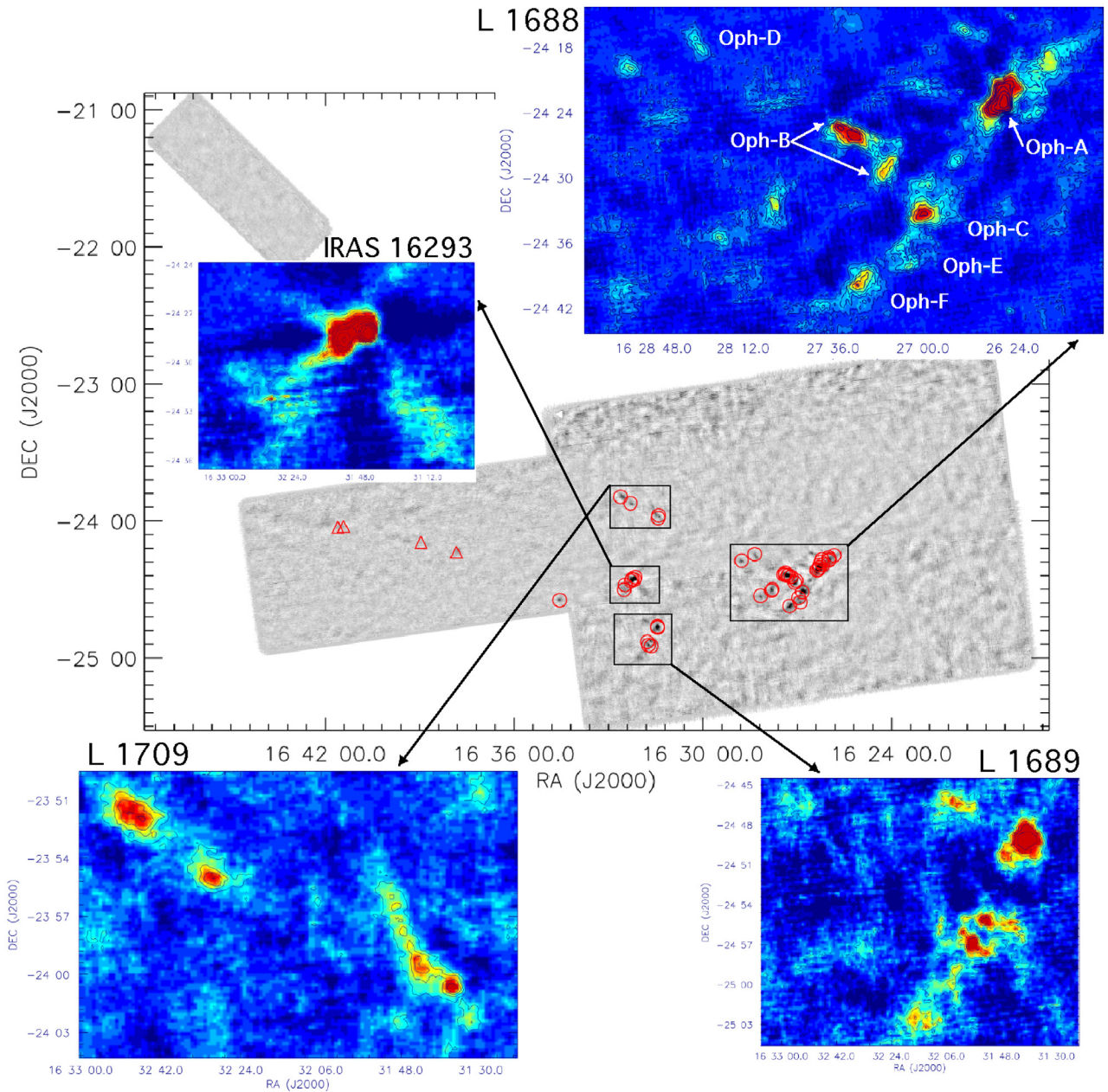


Figure 3.4 1.1 mm Bolocam map of the Ophiuchus molecular cloud, with the positions of the 44 sources detected above 4σ marked as circles. The gray scale shows the intensity *not* weighted by the coverage. The inset maps show particular regions on an expanded scale. The conversion from intensity to color differs among the insets to cover the large range of intensity. Sources marked by triangles in the eastern streamer are below the 4σ detection limit so are tentative detections (but see figure 3.5).

Visual comparison to previous maps of dust continuum emission in the L1688 cluster indicates reasonable agreement on the overall shape of the emission, considering differences in resolution (Motte et al., 1998) and wavelength (Johnstone et al., 2000). However, detailed comparison of source positions in table 3.1 and those in Johnstone et al. (2000) shows that a substantial number of our sources are separated into multiple sources by Johnstone et al. (2000), who used the the Clumpfind algorithm on data with better resolution by a factor of two; in the same area, they list 48 sources compared to our 23. The list of 48 includes some small, weak, but unconfused sources that we do not see. Assuming that $S_\nu \propto \nu^3$, as expected for emission in the Rayleigh-Jeans limit with an opacity proportional to ν , some of these sources should still lie above our detection limit, but not far above.

The Stanke et al. (2006) map covers 1.3 deg^2 of L1688 (slightly less than one of the boxes defined by the grid lines in figure 3.2), with lower noise ($\sim 10 \text{ mJy}$) and a slightly smaller beam ($24''$) at nearly the same wavelength (1.2 mm). Their images are qualitatively very similar to the L1688 inset image in figure 3.4. However, they find 143 sources in this region, using wavelet analysis and Clumpfind, and by essentially cleaning down to the noise. They include sources that are less than 3σ but extended. These differences make it difficult to compare sources in detail, but it appears that many of our sources would be split into multiple sources by Stanke et al. (2006).

Another useful comparison is with the work of Visser, Richer, & Chandler (2002) in a less crowded area of Ophiuchus. They found 5 sources along a filament in L1709; we find three sources in reasonable agreement in position, while L1709-SMM3 and L1709-SMM5 from their paper are blended into Bolo 30 in table 3.1. We see additional structure below the 4σ limit extending to the northeast of that group of sources that is not seen in the Visser et al. (2002) map. The most diffuse source in their map, L1709-SMM4, shows up strongly in our map, but shifted about $25''$ east, an example of position shifts caused by different sensitivity to large scale structure and source finding algorithms. Visser et al. (2002) also found a weak source in L1704 that we do not see, consistent with our detection limit. These points should be borne in mind when we compare source statistics to those of previous work in later sections.

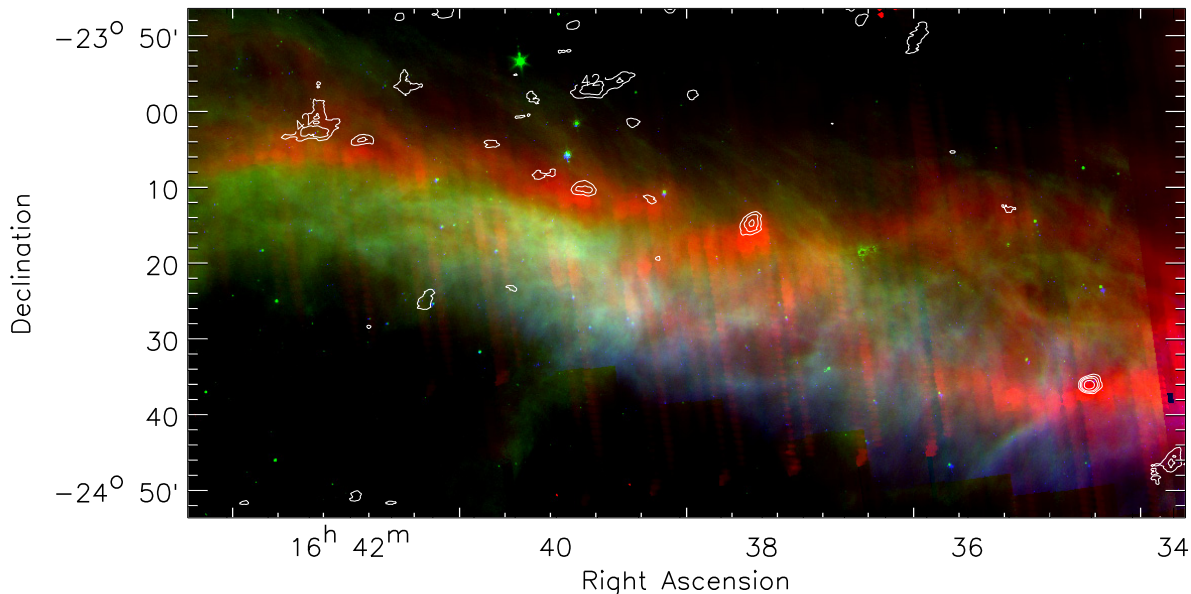


Figure 3.5 Emission at 1.1 mm seen with Bolocam in the eastern streamer (2, 3, 4, 6, 8 σ contours) is overlaid on a three color image from *Spitzer*, with IRAC band 4 (8 μm) in blue, MIPS band 1 (24 μm) in green, and MIPS band 3 (160 μm) in red. The 160 μm map is incompletely sampled and saturated emission produces stripes. The 160 μm map has been smoothed, but artifacts remain. The 1.1 mm emission does line up with the relatively opaque part of the streamer, as indicated by weak emission at 8 μm and strong emission at 160 μm .

Several diffuse emission peaks were observed in the eastern streamer, an area that includes L1712 ($16^h 38^m, -24^\circ 26'$) and L1729 ($16^h 43^m, -24^\circ 06'$). However, these cores, though visible by eye in the map, are only 3σ detections; they are listed separately as tentative detections in table 3.1, and are not included in our source statistics. These sources are in a long filament of extinction that extends east from the main cloud (Cambr sy 1999; Ridge et al. 2006). We believe at least some of these sources are real, based on inspection by eye and comparison to *Spitzer* maps of the region. In figure 3.5, the tentative 1.1 mm sources align with an elongated structure that is dark at 8 μm , but bright at 160 μm , suggestive of a cold, dense filament. This filament was previously observed in ^{13}CO (Loren, 1989) and C^{18}O (Tachihara et al., 2000), but it has not been mapped in the millimeter continuum until now. While the overall morphology is similar to that seen in C^{18}O (Tachihara et al., 2000), only

Bolo 45 has an obvious counterpart, ρ -Oph 10, in the table of Tachihara et al. (2000).

The most striking feature of the Bolocam map of Ophiuchus is the lack of 1.1 mm emission in regions outside of known regions of star formation, even in areas with significant extinction ($A_V > 3$ mag). Figure 3.6 shows the Bolocam map of Ophiuchus overlaid with extinction contours constructed using the *NICE* method (e.g., Lada, Alves, & Lada 1999; Huard et al. 2006), making use of 2MASS sources, and convolving the line-of-sight extinctions with a Gaussian beam with FWHM of $5'$. This method depends on background stars to probe the column densities through the cloud (see also §2.4.2) In order to calibrate the extinction map, we identified two “off-cloud” regions, which were free of structure and assumed to be non-extincted regions near the Ophiuchus cloud. These off-cloud regions contained a total of more than 13,000 stars and were 0.6×0.6 and 1.5×0.2 fields centered on $\alpha = 16^h 44^m 00^s$, $\delta = -22^\circ 54' 00''$ and $\alpha = 16^h 39^m 12^s$, $\delta = -25^\circ 24' 00''$ (J2000.0), respectively. The mean intrinsic H–K color of the stars in these off-cloud fields was found to be 0.190 ± 0.003 magnitudes. We assume $A_V = 15.9 E(H-K)$ to convert to A_V (Rieke & Lebofsky, 1985).

The 1.1 mm sources are all in regions of high extinction, but not all regions of substantial extinction have Bolocam sources. For example, we found no 1.1 mm sources in the small northeastern streamer of Ophiuchus that could be confirmed as real by eye despite having much lower noise in this region than for the rest of the map. The beam-averaged extinctions in the northeastern streamer are $A_V \approx 3$ to 8 magnitudes. The 4σ detection limit in this region corresponds to objects with masses as small as $0.06 M_\odot$ (see §3.4.2). Thus even in relatively high extinction regions, much of the Ophiuchus cloud appears devoid of dense cores down to a very low mass limit.

3.4.2 Source Properties

3.4.2.1 Positions and Photometry

Table 3.1 lists the position, peak flux density, and signal-to-noise ratio (S/N) of the 44 4σ sources, with the four 3σ detections in the eastern streamer are listed separately.

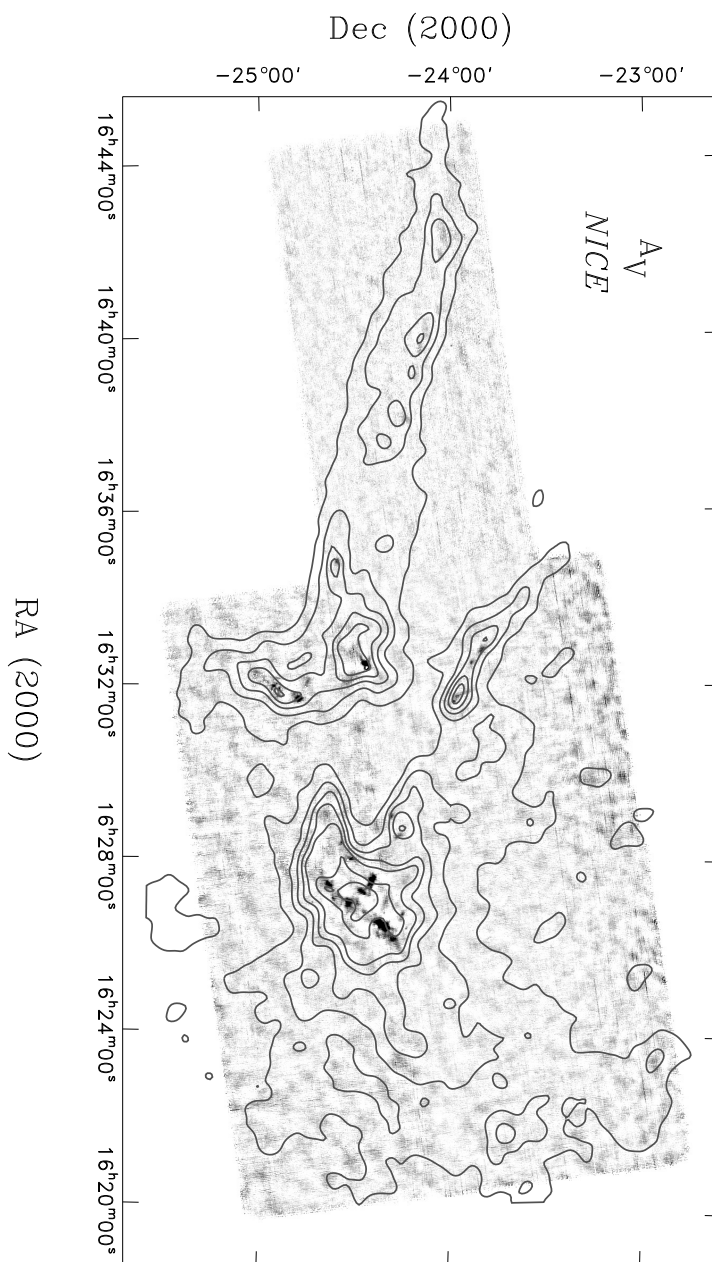


Figure 3.6 Visual extinction (A_V) contours calculated from 2MASS data using the *NICE* method, overlaid on the grayscale 1.1 mm map. Contours are $A_V = 2, 4, 6, 8, 10, 15,$ and 20 mag with an effective resolution of $5'$.

All statistical analysis is based on the 44 secure detections only. For known sources the most common names from the literature are also given. Some are known to host protostars while others may be starless. The uncertainty in the peak flux density is the local rms beam $^{-1}$ and does not include an additional 15% systematic uncertainty.

Table 3.1. Identified sources in Ophiuchus

ID	RA (2000) (h m s)	Dec (2000) (° ' ")	Peak (Jy/beam)	S/N	other names
Bolo 1	16 25 59.1	-24 18 16.2	0.26 (0.03)	4.5	
Bolo 2	16 26 08.1	-24 20 00.6	0.39 (0.03)	4.7	CRBR 2305.4-1241?
Bolo 3	16 26 09.6	-24 19 15.6	0.31 (0.03)	4.1	SMM J16261-2419 (1)
Bolo 4	16 26 09.9	-24 20 28.6	0.40 (0.03)	6.2	GSS26?
Bolo 5	16 26 20.7	-24 22 17.0	0.37 (0.04)	4.3	GSS30-IRS3 (2); SMM J16263-2422 (1); LFAM1 (3)
Bolo 6	16 26 22.9	-24 20 00.9	0.27 (0.03)	4.5	SMM J16263-2419 (1)
Bolo 7	16 26 24.7	-24 21 07.5	0.41 (0.04)	4.9	A-MM4? (5)
Bolo 8	16 26 27.2	-24 22 26.7	1.38 (0.04)	16.0	SM1 FIR1 (4); A-MM5/6? (5); SMM J16264-2422 (1)
Bolo 9	16 26 27.6	-24 23 36.6	2.70 (0.04)	45.2	SM1 FIR2 (4); SM1N
Bolo 10	16 26 29.7	-24 24 28.8	2.66 (0.04)	47.5	SM2
Bolo 11	16 26 32.6	-24 24 45.3	1.25 (0.04)	14.8	A-MM8 (5)
Bolo 12	16 27 00.7	-24 34 17.0	0.54 (0.03)	8.4	SMM J16269-2434 (1); C-MM3 (5)
Bolo 13	16 27 04.3	-24 38 47.4	0.23 (0.03)	4.8	E-MM2d (5); SMM J16270-2439 (1)
Bolo 14	16 27 07.9	-24 36 54.3	0.26 (0.03)	4.4	SMM J16271-2437a/b (1); Elias29?
Bolo 15	16 27 12.2	-24 29 18.9	0.44 (0.04)	6.1	B1-MM2/3 (5); IRAS 16242-2422; SMM J16272-2429 (1)
Bolo 16	16 27 15.1	-24 30 12.6	0.45 (0.04)	7.1	SMM J16272-2430 (1); B1-MM4 (5)
Bolo 17	16 27 22.3	-24 27 36.3	0.40 (0.04)	4.4	B2-MM4 (5)
Bolo 18	16 27 25.2	-24 40 28.9	0.47 (0.03)	9.7	F-MM2 (5); IRS43? (5)
Bolo 19	16 27 27.0	-24 26 57.1	0.62 (0.04)	7.4	SMM J16274-2427s (1)
Bolo 20	16 27 29.1	-24 27 11.1	0.69 (0.04)	9.4	B2-MM8 (5); SMM J16274-2427b (1)
Bolo 21	16 27 33.1	-24 26 48.8	0.53 (0.04)	6.8	B2-MM15 (5); SMM J16275-2426 (1)
Bolo 22	16 27 33.4	-24 25 57.3	0.50 (0.03)	9.4	B2-MM13 (5); SMM J16275-2426 (1)
Bolo 23	16 27 36.7	-24 26 36.2	0.40 (0.03)	5.1	B2-MM17 (5)
Bolo 24	16 27 58.3	-24 33 09.7	0.29 (0.03)	6.0	
Bolo 25	16 28 00.1	-24 33 42.8	0.33 (0.03)	6.0	H-MM1 (8)
Bolo 26	16 28 21.0	-24 36 00.0	0.23 (0.03)	5.5	
Bolo 27	16 28 32.1	-24 17 43.4	0.17 (0.03)	4.1	D-MM3/4 (5)
Bolo 28	16 28 57.7	-24 20 33.7	0.28 (0.03)	5.8	I-MM1 (8)
Bolo 29	16 31 36.4	-24 00 41.7	0.28 (0.03)	7.0	L1709-SMM1 (6); IRS63
Bolo 30	16 31 37.2	-24 01 51.9	0.29 (0.03)	6.3	L1709-SMM3,5 (6)
Bolo 31	16 31 40.0	-24 49 58.0	0.45 (0.03)	6.8	
Bolo 32	16 31 40.4	-24 49 26.4	0.45 (0.03)	7.4	
Bolo 33	16 31 52.6	-24 58 00.8	0.20 (0.03)	4.5	
Bolo 34	16 31 58.0	-24 57 38.8	0.26 (0.03)	5.2	
Bolo 35	16 32 00.6	-24 56 13.9	0.19 (0.03)	4.5	IRAS 16289-2450; L1689S; IRS67
Bolo 36	16 32 22.5	-24 27 47.5	1.65 (0.03)	17.9	

Source photometry is presented in table 3.2, which gives flux densities within set apertures of 40", 80", and 120", as well as the best-estimate total flux density. Only apertures smaller than the distance to the nearest neighboring source are used, to avoid contamination from neighboring sources. The total flux density is calculated in the largest aperture (up to 160") that does not include flux from nearby sources. Uncertainties in table 3.2 do not include an additional 15% systematic uncertainty.

Table 3.1 (cont'd)

ID	RA (2000) (h m s)	Dec (2000) (° ' ")	Peak (Jy/beam)	S/N	other names
Bolo 37	16 32 24.7	-24 28 51.2	3.03 (0.03)	80.7	IRAS 16293-2422
Bolo 38	16 32 28.6	-24 28 37.5	1.07 (0.03)	17.0	
Bolo 39	16 32 30.1	-23 55 18.4	0.25 (0.03)	4.8	L1709-SMM2 (6)
Bolo 40	16 32 30.8	-24 29 28.3	0.74 (0.03)	14.7	
Bolo 41	16 32 42.3	-24 31 13.0	0.15 (0.02)	4.5	
Bolo 42	16 32 44.1	-24 33 21.6	0.20 (0.03)	4.3	
Bolo 43	16 32 49.2	-23 52 33.9	0.28 (0.03)	4.1	L1709-SMM4? (6); LM182
Bolo 44	16 34 48.3	-24 37 24.6	0.21 (0.02)	5.6	L1689B-3
Tentative detections in the eastern streamer					
Bolo 45	16 38 07.8	-24 16 36.4	0.15 (0.02)	3.6	ρ -Oph 10 (7)
Bolo 46	16 39 15.8	-24 12 20.8	0.10 (0.02)	3.2	
Bolo 47	16 41 44.5	-24 05 20.4	0.14 (0.02)	3.0	
Bolo 48	16 41 55.6	-24 05 41.6	0.12 (0.02)	3.0	

Note. — Numbers in parentheses are 1σ errors. The peak flux density is the peak pixel value in the $10''$ pixel $^{-1}$ unfiltered map (without the Wiener filter applied). The uncertainty in the peak flux density is the local (calculated within a $400''$ box) rms beam $^{-1}$, calculated from the noise map, and does not include an additional 15% systematic uncertainty from calibration uncertainties and residual errors after iterative mapping. Other names listed are the most common identifications from the literature, and are not meant to be a complete list. References – (1) Johnstone et al. 2000; (2) Castelaz et al. 1985; Weintraub et al. 1993; (3) Leous et al. 1991; (4) Mezger et al. 1992; (5) Motte et al. 1998; (6) Visser et al. 2002; (7) Tachihara et al. 2000; (8) Johnstone et al. 2004

Table 3.2. Photometry, masses, sizes, and morphology for sources in Ophiuchus

ID	Flux(40'') (Jy)	Flux(80'') (Jy)	Flux(120'') (Jy)	Total Flux (Jy)	Mass (10K) (M_{\odot})	Peak A_V (mag)	FWHM (minor, '')	FWHM (major, '')	PA ($^{\circ}$)	$\langle n \rangle$ cm^{-3}	Morphology ¹
Bolo1	0.34 (0.03)	0.82 (0.07)	1.55 (0.1)	2.13 (0.13)	1.29 (0.08)	18	88 (0.9)	133 (1.4)	-24 (2)	2×10^5	multiple, extended, round
Bolo2	0.46 (0.03)	0.28 (0.02)	27	55 (0.6)	58 (0.6)	29 (17)	4×10^5	multiple, round
Bolo3	0.46 (0.04)	0.58 (0.05)	0.35 (0.03)	22	53 (0.7)	58 (0.8)	88 (10)	5×10^5	multiple, extended, round
Bolo4	0.49 (0.03)	0.3 (0.02)	28	52 (0.6)	56 (0.7)	-10 (11)	5×10^5	multiple, elongated
Bolo5	0.55 (0.05)	1.32 (0.1)	...	1.61 (0.11)	0.97 (0.07)	26	64 (0.8)	70 (0.8)	26 (11)	7×10^5	multiple, extended, elongated
Bolo6	0.32 (0.05)	0.58 (0.08)	0.35 (0.05)	19	59 (1.3)	67 (1.5)	-61 (14)	3×10^5	multiple, extended, weak
Bolo7	0.56 (0.05)	1.08 (0.08)	0.65 (0.05)	29	56 (0.6)	66 (0.8)	-50 (6)	7×10^5	multiple, extended, elongated
Bolo8	1.86 (0.05)	3.93 (0.09)	2.37 (0.05)	98	55 (0.2)	63 (0.2)	81 (2)	3×10^6	multiple, extended, round
Bolo9	4.2 (0.05)	6.49 (0.08)	3.92 (0.05)	191	46 (0.1)	56 (0.1)	-68 (1)	9×10^6	multiple, extended, round
Bolo10	3.42 (0.05)	3.42 (0.05)	2.07 (0.03)	189	44 (0.1)	56 (0.1)	22 (1)	5×10^6	multiple, extended, round
Bolo11	1.72 (0.05)	1.72 (0.05)	1.04 (0.03)	88	49 (0.2)	54 (0.2)	50 (3)	2×10^6	multiple, extended, round
Bolo12	0.86 (0.04)	2.11 (0.09)	3.91 (0.13)	5.56 (0.17)	3.36 (0.1)	38	105 (0.5)	125 (0.6)	-45 (2)	4×10^5	extended, elongated
Bolo13	0.35 (0.04)	0.75 (0.08)	1.35 (0.12)	1.35 (0.12)	0.82 (0.07)	16	76 (1.2)	96 (1.5)	44 (5)	2×10^5	multiple, extended, elongated, weak
Bolo14	0.32 (0.05)	0.68 (0.09)	1.19 (0.14)	1.19 (0.14)	0.72 (0.08)	18	66 (1.2)	108 (2.)	41 (3)	2×10^5	multiple, extended, weak
Bolo15	0.61 (0.05)	0.92 (0.07)	0.56 (0.04)	31	50 (0.7)	64 (0.8)	19 (4)	8×10^5	multiple, extended, elongated
Bolo16	0.7 (0.05)	1.08 (0.07)	0.65 (0.04)	32	51 (0.6)	62 (0.7)	-58 (5)	9×10^5	multiple, extended, elongated
Bolo17	0.54 (0.05)	1.03 (0.09)	0.62 (0.06)	29	56 (0.8)	68 (1.)	-62 (6)	6×10^5	multiple, extended, elongated
Bolo18	0.65 (0.04)	1.49 (0.08)	2.64 (0.11)	3.76 (0.15)	2.27 (0.09)	33	96 (0.6)	149 (1.)	41 (1)	2×10^5	extended, elongated
Bolo19	0.8 (0.04)	0.48 (0.02)	44	54 (0.4)	58 (0.4)	-8 (9)	7×10^5	multiple, round
Bolo20	0.87 (0.04)	0.53 (0.02)	49	51 (0.4)	57 (0.4)	80 (6)	9×10^5	multiple, extended, round
Bolo21	0.82 (0.04)	1.01 (0.06)	0.61 (0.03)	37	53 (0.5)	60 (0.5)	40 (5)	9×10^5	multiple, extended, round
Bolo22	0.77 (0.04)	0.96 (0.06)	0.58 (0.03)	35	54 (0.5)	55 (0.5)	-75 (61)	10×10^5	multiple, extended, elongated
Bolo23	0.55 (0.04)	0.68 (0.05)	0.41 (0.03)	28	53 (0.6)	56 (0.7)	-88 (20)	7×10^5	multiple, extended, round

Table 3.2 (cont'd)

ID	Flux(40'') (Jy)	Flux(80'') (Jy)	Flux(120'') (Jy)	Total Flux (Jy)	Mass (10K) (M_{\odot})	Peak A_V (mag)	FWHM (minor, '')	FWHM (major, '')	PA ($^{\circ}$)	(n) cm $^{-3}$	Morphology ¹
Bolo24	0.39 (0.04)	0.39 (0.04)	0.24 (0.02)	21	48 (0.8)	57 (0.9)	14 (7)	5×10^5	multiple, extended, elongated
Bolo25	0.39 (0.04)	0.39 (0.04)	0.24 (0.02)	23	47 (0.8)	56 (0.9)	-66 (7)	5×10^5	multiple, elongated
Bolo26	0.3 (0.03)	0.63 (0.07)	1.14 (0.1)	1.62 (0.14)	0.98 (0.08)	16	108 (1.4)	132 (1.8)	84 (5)	9×10^4	extended, elongated
Bolo27	0.23 (0.03)	0.52 (0.07)	0.97 (0.1)	1.48 (0.13)	0.9 (0.08)	12	89 (1.1)	157 (2.)	58 (2)	2×10^4	extended, elongated, weak
Bolo28	0.37 (0.03)	0.86 (0.07)	1.55 (0.1)	2.17 (0.13)	1.31 (0.08)	20	102 (1.)	113 (1.1)	74 (8)	2×10^5	extended, elongated
Bolo29	0.28 (0.04)	0.5 (0.07)	0.3 (0.04)	20	54 (1.)	57 (1.1)	11 (29)	5×10^5	multiple, extended, elongated
Bolo30	0.28 (0.04)	0.46 (0.06)	0.28 (0.04)	20	46 (1.1)	57 (1.3)	66 (9)	6×10^5	multiple, extended, elongated
Bolo31	0.55 (0.03)	0.33 (0.02)	32	54 (0.5)	57 (0.5)	-61 (15)	5×10^5	multiple, round
Bolo32	0.53 (0.03)	0.32 (0.02)	31	56 (0.5)	58 (0.5)	74 (20)	4×10^5	multiple, round
Bolo33	0.26 (0.04)	0.57 (0.07)	...	0.57 (0.07)	0.35 (0.04)	14	54 (1.2)	65 (1.5)	-33 (10)	4×10^5	multiple, extended, elongated, weak
Bolo34	0.38 (0.04)	0.87 (0.08)	...	0.87 (0.08)	0.52 (0.05)	19	59 (0.9)	68 (1.1)	-73 (9)	4×10^5	multiple, extended, elongated
Bolo35	0.22 (0.04)	0.39 (0.08)	...	0.46 (0.09)	0.28 (0.06)	13	66 (1.7)	77 (2.1)	40 (14)	2×10^5	multiple, extended, elongated, weak
Bolo36	1.35 (0.04)	2.49 (0.07)	1.51 (0.04)	117	53 (0.2)	57 (0.2)	-17 (5)	2×10^6	multiple, extended, round
Bolo37	3.63 (0.04)	4.47 (0.06)	2.7 (0.04)	214	35 (0.1)	45 (0.1)	49 (1)	3×10^7	multiple, round
Bolo38	1.52 (0.04)	2.33 (0.06)	1.41 (0.04)	76	54 (0.2)	54 (0.2)	-15 (38)	2×10^6	multiple, extended, round
Bolo39	0.26 (0.04)	0.55 (0.07)	0.94 (0.11)	1.29 (0.14)	0.78 (0.08)	17	101 (1.7)	128 (2.2)	-51 (6)	9×10^4	extended
Bolo40	1.11 (0.04)	1.67 (0.06)	1.01 (0.04)	52	49 (0.3)	58 (0.3)	55 (3)	2×10^6	multiple, extended, round
Bolo41	0.2 (0.03)	0.39 (0.06)	0.73 (0.09)	0.85 (0.1)	0.51 (0.06)	11	40 (1.2)	53 (1.6)	-27 (9)	2×10^6	multiple, extended, elongated, weak
Bolo42	0.19 (0.03)	0.39 (0.07)	0.72 (0.1)	0.83 (0.11)	0.5 (0.07)	14	53 (1.6)	66 (1.9)	80 (11)	6×10^5	multiple, extended, elongated, weak
Bolo43	0.33 (0.04)	0.84 (0.07)	1.63 (0.11)	2.45 (0.15)	1.48 (0.09)	20	98 (0.9)	143 (1.3)	47 (2)	1×10^5	extended, elongated
Bolo44	0.3 (0.03)	0.72 (0.06)	1.21 (0.09)	1.71 (0.12)	1.03 (0.08)	15	96 (1.1)	119 (1.4)	55 (4)	1×10^5	extended, round
Tentative detections in the eastern streamer											
Bolo45	0.20 (0.03)	0.47 (0.06)	0.94 (0.09)	1.36 (0.11)	0.82 (0.06)	11	123 (1.5)	157 (1.9)	-51 (4)	5×10^4	extended, elongated, weak

Table 3.2 (cont'd)

ID	Flux(40'')	Flux(80'')	Flux(120'')	Total Flux (Jy)	Mass (10K) (M_{\odot})	Peak A_V (mag)	FWHM (minor, '')	FWHM (major, '')	PA ($^{\circ}$)	$\langle n \rangle$ cm^{-3}	Morphology ¹
Bolo46	0.08 (0.02)	0.05 (0.01)	7	64 (3)	153 (6)	7 (3)	9×10^3	extended, round, weak
Bolo47	0.13 (0.03)	0.15 (0.04)	0.09 (0.02)	10	87 (2)	112 (3)	-42 (9)	2×10^4	multiple, extended, round, weak
Bolo48	0.86 (0.13)	0.52 (0.08)	8	84 (2)	111 (3)	-8 (7)	1×10^5	multiple, extended, round, weak

Note. — Masses are calculated according to equation (2.3) from the total flux density assuming a single dust temperature of $T_D = 10K$ and a dust opacity at 1.1mm of $\kappa_{1.1mm} = 0.0114 \text{ cm}^2 \text{ g}^{-1}$. Peak A_V is calculated from the peak flux density as in equation (2.2). FWHM and PAs are from a Gaussian fit; the PA is measured in degrees east of north of the major axis. $\langle n \rangle$ is the mean particle density as calculated from the total mass and the deconvolved average FWHM size. Numbers in parentheses are 1σ uncertainties. Uncertainties for masses are from photometry only, and do not include uncertainties from κ , T_D , or d , which can be up to a factor of a few or more. Uncertainties for the FWHM and PA are formal fitting errors from the elliptical Gaussian fit; additional uncertainties of 10% – 15% apply to the FWHM, and $\sim 5^{\circ}$ to the PA (determined from simulations).

¹The morphology keyword(s) given indicates whether the source is multiple (within $3'$ of another source), extended (major axis FW at $2\sigma > 1'$), elongated (axis ratio at $4\sigma > 1.2$), round (axis ratio at $4\sigma < 1.2$), or weak (peak flux densities less than 8.7 times the rms beam $^{-1}$).

The distribution of flux densities for the 44 detected sources is shown in figure 3.7. This figure compares the distribution of peak flux densities to the total flux densities. The peak flux density distribution has a mean of $\sim 0.6 \text{ Jy beam}^{-1}$. The total flux density distribution has a mean of about 1.6 Jy . The shaded region in figure 3.7 indicates the 4σ detection limit, which varies throughout the map from $\sim 0.06 - 0.12 \text{ Jy beam}^{-1}$. The flux density distributions shown in figure 3.7 are similar to the distributions of peak and total flux densities of Bolocam sources in Perseus (chapter 2) in that the total flux density distribution is shifted from the peak distribution because most sources are larger than the beam.

3.4.2.2 Sizes and Shapes

Sizes and position angles (PA) in table 3.2 were found by fitting a 2D elliptical Gaussian to each source. The size of any given source is limited by the distance to its nearest neighbor, because emission at radii greater than half the distance to the nearest source is masked out for the Gaussian fit. This method also ensures that the size and the total flux density of a source are measured in approximately the same aperture. The sources in the L1688 cluster are quite crowded and source sizes and fluxes may be affected by nearby sources.

Figure 3.8 shows the distributions of source major and minor axis FWHMs. Both distributions peak between $50''$ and $60''$, and the average axis ratio is 1.2. Only a few sources have large FWHM sizes larger than $100''$. Many of the sources in the map are part of more extended structures. Large clumps of emission can be broken into several smaller sources by our source-finding routine if the clumps contain several local peaks. Our method of finding cores and the filamentary nature of the dense gas in Ophiuchus could result in a slight elongation of the sources. However, the majority (61%) of sources in the entire sample are not elongated at the half-max contour (axis ratio < 1.2).

Morphology keywords for each source are also listed in table 3.2. Of the 44 sources, 18 are classified as round, with axis ratio at the 4σ level less than 1.2. The difference between this result and the fact that 61% had axis ratios from the Gaussian fits < 1.2

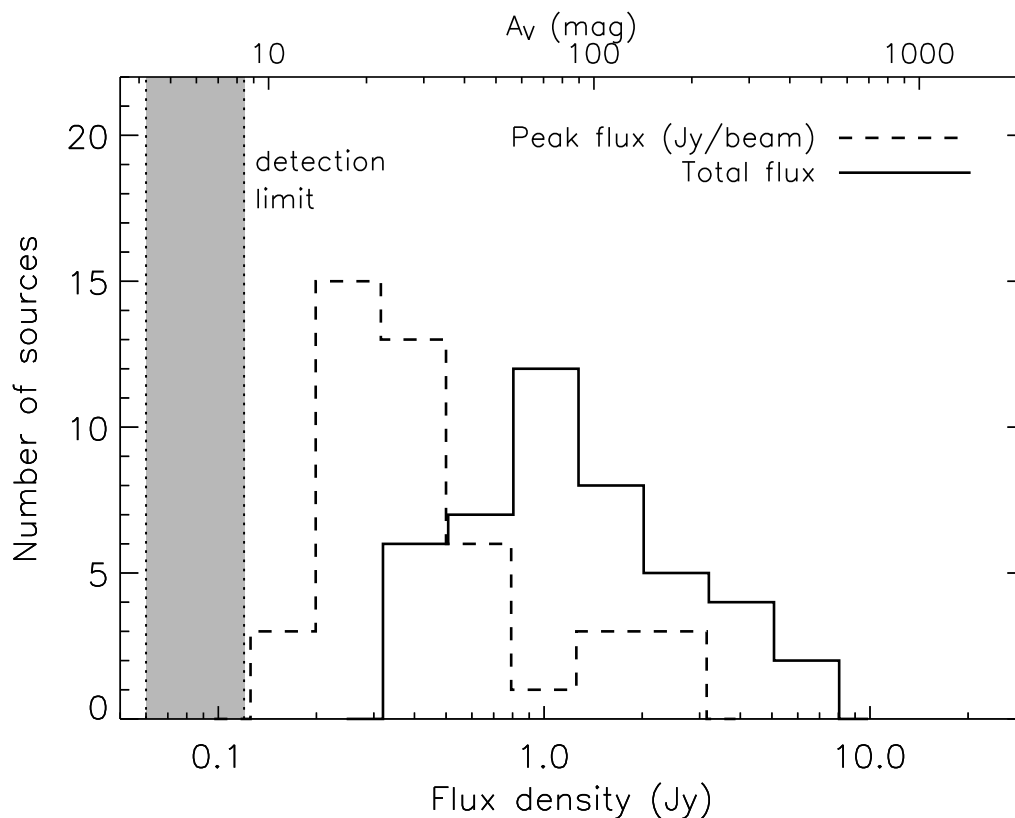


Figure 3.7 The distribution of the peak flux densities (dashed line) and total flux densities (solid line) of the 4σ sources. The peak flux density is the peak pixel value in the map, in Jy beam^{-1} . The top axis shows the value of A_V inferred from the emission, using equation (2.2). The mean peak flux density of the sample is 0.6 Jy/beam and the mean total flux is 1.6 Jy . The 4σ detection limit varies from 0.06 to 0.12 Jy/beam across the map due to variations in the local noise, although most sources are detected in the higher noise regions. The range in noise is indicated by the shaded region.

suggests spherical sources embedded along more elongated filamentary structures. Visual inspection indicates that at lower contours sources are usually elongated along the local filamentary structure, as seen both in the still lower contours and in the extinction map (figure 3.6). Future polarimetric observations could determine the role of magnetic fields in the filamentary structures.

Of the 44 sources, 36 are multiple, reflecting the strongly clustered nature of the sources (see §3.5.3). Also 36 sources are extended. Only two sources are neither multiple nor extended. We see no evidence for a population of isolated, small, dense

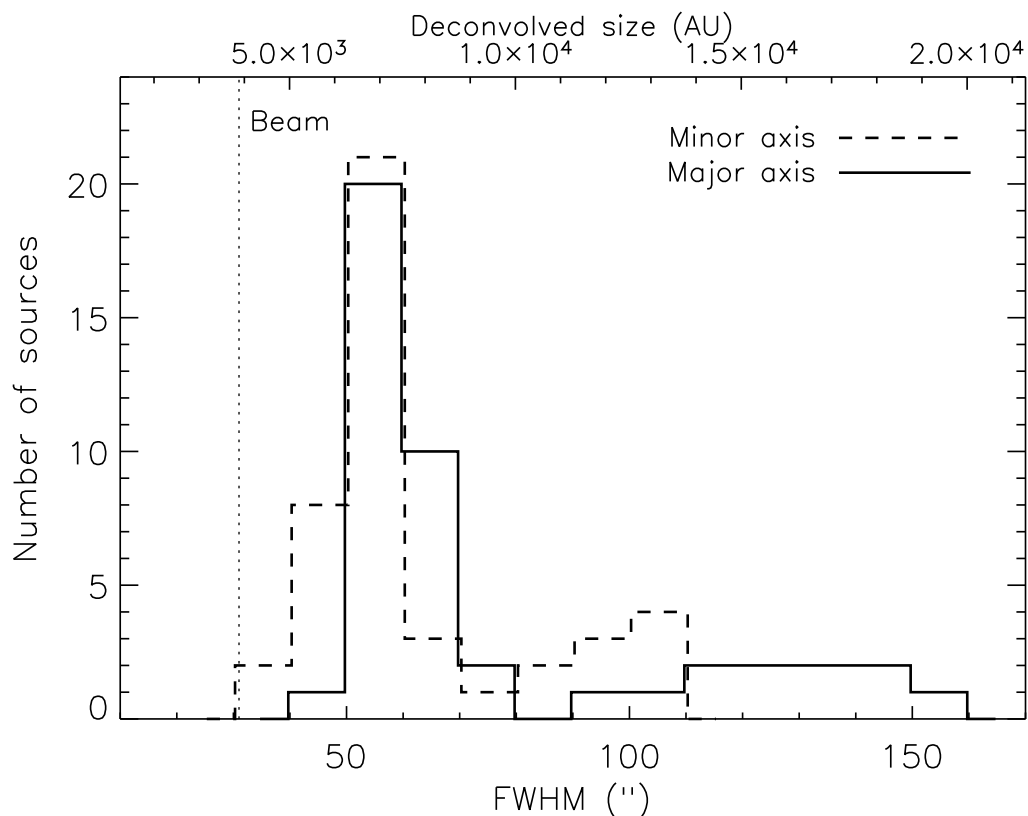


Figure 3.8 The distribution of source FWHM minor axis (dashed line) and major axis (solid line), as determined from an elliptical Gaussian fit. The beam size is indicated by the dotted line. The mean FWHM sizes of the sample are $62''$ (minor) and $77''$ (major). The top axis gives deconvolved sizes in AU, assuming a $31''$ beam and $d = 125$ pc.

cores.

3.4.2.3 Masses, Densities, and Extinctions

Isothermal masses were calculated as in chapter 2 (equation (2.3)), and are listed in table 3.2. Uncertainties in the masses are from the uncertainty in the total flux density only and do not include uncertainties in distance, opacity, and T_D , which combined can be at least a factor of 4. The total mass of the 44 4σ sources is $42 M_\odot$, with a mean of $0.96 M_\odot$, and a range from 0.24 to $3.9 M_\odot$. The Johnstone et al. (2004) survey of Ophiuchus found a larger total mass ($50 M_\odot$) in a smaller area than we covered. Those authors assumed a larger distance (160 pc), a value for κ_ν

at $850\ \mu\text{m}$ that is 1.1 times higher than OH5 dust, and $T_D = 15\ \text{K}$. If we used the assumptions of Johnstone et al. (2004) for our data, we would derive a total mass of $32\ M_\odot$ from our data. The source of the difference between our result for total mass in cores and that of Johnstone et al. (2004) does not seem to be explained by the assumptions used to obtain mass. More likely, it arises from differences in methods of defining sources. If we integrate all the areas of the map above 4σ , we get $131\ \text{Jy}$, which translates to $79\ M_\odot$, using our usual assumptions, or $60\ M_\odot$, using the assumptions of Johnstone et al. (2004). Thus about half the mass traced by $1.1\ \text{mm}$ emission cannot be assigned to a particular core, primarily because it is in confused regions.

de Geus et al. (1989) estimate a mass for the whole Ophiuchus cloud of $10^4\ M_\odot$ while we find $2300\ M_\odot$ above $A_V = 2$. We calculate the cloud mass using the 2MASS extinction map and a conversion from A_V to column density of $N(\text{H}_2)/A_V = 0.94 \times 10^{21}\ \text{mag cm}^{-2}$ (Bohlin, Savage, & Drake, 1978). Thus the percentage of cloud mass in dense cores is between 0.4% and 1.8%. This fraction is even lower than that found in chapter 2 for Perseus (between 1% and 3%).

Mean densities (calculated as in §2.4.3) are quite high compared to the surrounding cloud, ranging from $\langle n \rangle = 9 \times 10^4\ \text{cm}^{-3}$ to $3 \times 10^7\ \text{cm}^{-3}$, with an average value of $1.6 \times 10^6\ \text{cm}^{-3}$. The free-fall timescale estimated from this mean density is only $2.7 \times 10^4\ \text{yr}$. Peak extinctions calculated from the peak $1.1\ \text{mm}$ flux density (table 3.2 and figure 3.7) range from $A_V = 11$ to $214\ \text{mag}$ for the 4σ sources, with a mean value of $43\ \text{mag}$. Values for the tentative detections in the eastern streamer range from $A_V = 7$ to $11\ \text{mag}$.

Peak extinctions within the cores should be distinguished from the surrounding cloud extinction as traced by the 2MASS extinction map. While reddened 2MASS sources probe low-to-moderate extinctions within the Ophiuchus cloud, the sensitivity of the 2MASS observations is not sufficient to probe reliably the high extinction regions traced by the millimeter emission. By considering both tracers of extinction, the morphology of the cloud can be inferred over a large range of column densities, from the diffuse and vast regions of the cloud (containing most of the mass) to the

densest cores. A quantitative comparison between 1.1 mm cores and cloud extinction will be made in §3.5.4.

3.5 Discussion

3.5.1 Completeness

Figure 3.9 shows the distribution of source mass versus size, where the size is the geometric average of the major and minor FWHM for each source. The minimum detectable mass and source size are related because we detect sources from their peak flux density, but calculate the mass from the total flux density. Therefore, we are biased against detecting large, faint, low-mass sources. For Gaussian sources, the mass detection limit as a function of size is simply related to the point source detection limit:

$$M_{lim}(\theta_s) = M_{lim}^{ps} (\theta_s/\theta_b)^2 [1 - \exp(-4 \ln 2 (120/\theta_s)^2)], \quad (3.1)$$

where M_{lim}^{ps} is the detection limit for a point source, and θ_s and θ_b are the FWHM of source and beam, respectively. The last factor corrects for flux from sources larger than our largest aperture, but has very little effect except at the largest sizes. This Gaussian completeness curve (which is essentially a line with $M \propto R^2$, where R is the radius) is plotted in the middle panel of figure 3.9 (solid lines). The two lines represent the range in rms over the map.

The real mass completeness limit is more complicated, even for Gaussian sources, as a result of the reduction and detection processes applied to the data. Empirical 10%, 50%, and 90% completeness limits are also plotted in figure 3.9 (bottom, middle, and top panels, respectively). These limits were determined by introducing simulated sources with a range of masses and sizes (from 30'' to 100'') into a portion of the Ophiuchus data with no real, then processing the map identically to the real data, as described in §2.5.1. The resulting completeness limits indicate what percentage of simulated sources with a particular size and mass were detected above 4σ in the

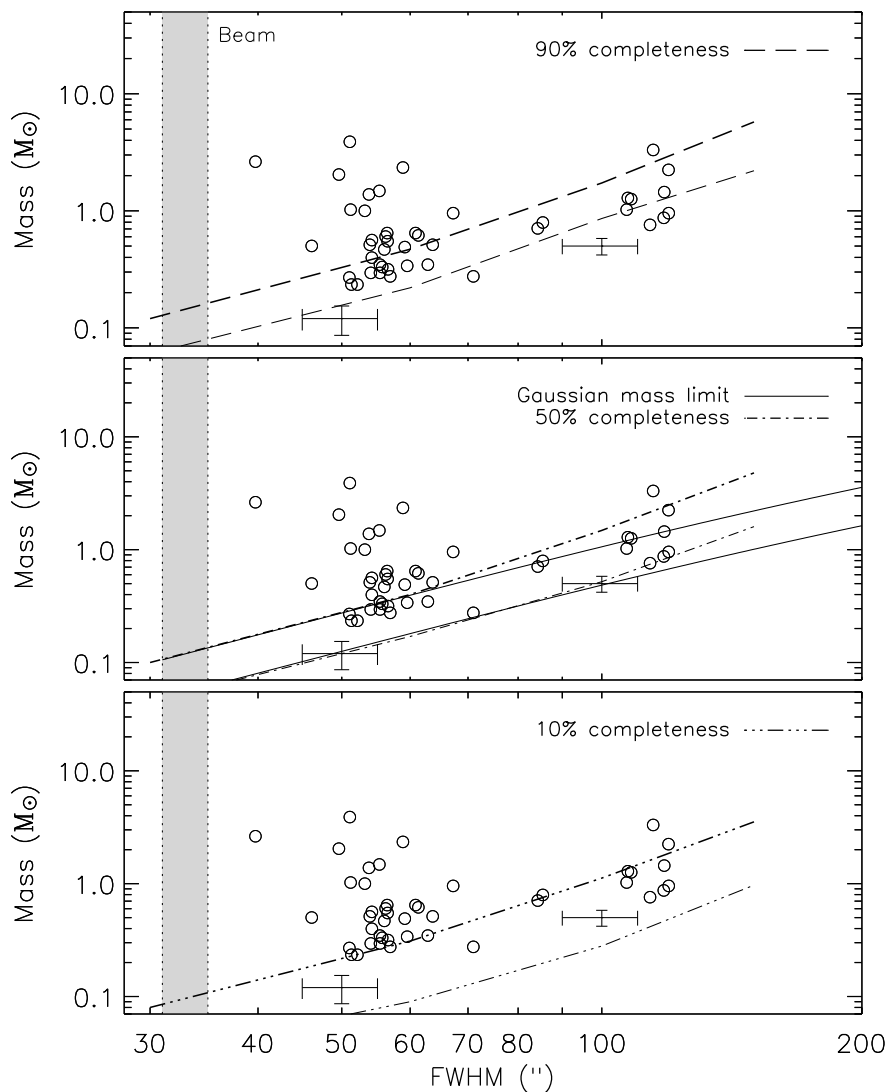


Figure 3.9 Distribution of source mass versus FWHM size. The size is the geometric average of the FWHM of the major and minor axes as given in table 3.1. The maximum size of the pointing-smear beam is represented by the shaded regions. Solid lines are the 50% analytic mass detection limit as a function of size for Gaussian sources (equation (3.1)). Empirical 90% (top panel), 50% (middle panel), and 10% (bottom panel) completeness limits are indicated, derived using Monte Carlo methods with simulated sources and taking into account the effects of cleaning, iterative mapping, and optimal filtering. Each completeness limit is calculated both in a low rms region (lower line) and a high rms region (upper line). Most real sources are found in the higher rms regions. Representative error bars for 50'' and 100'' FWHM sources near the detection limit are shown, as estimated from Monte Carlo simulations.

Wiener-convolved map. Because the local rms varies substantially across the map, completeness limits have been calculated both in low rms (20 mJy beam⁻¹, lower line in each panel) and high rms (25 to 30 mJy beam⁻¹, upper line) regions.

Most of the 44 sources are found in the higher rms regions of the map, corresponding to the upper curves in figure 3.9. Some of this noise is caused by mapping artifacts near strong sources (figure 3.3). Very large sources (FWHM > 100'') are not fully recovered by the iterative mapping routine (see chapter 2), and therefore tend to have a higher mass limit than expected for a simple scaling with source size. This is illustrated in the middle panel of figure 3.9, where the empirical completeness limit (dash-dot line) rises above the Gaussian limit (solid line) for large sources. Typical 1 σ error bars in M and FWHM are shown for 50'' and 100'' FWHM sources near the detection limit. The uncertainty in mass is from the uncertainty in the integrated flux (including the 5% uncertainty from the cleaning process, but not the absolute calibration uncertainty), and the uncertainty in size is estimated from simulations.

The distribution of source mass versus size values in figure 3.9 does not look like a distribution of constant density cores of varying sizes ($M \propto R^3$), nor like a collection of cores with constant column density ($M \propto R^2$). Rather, it looks as if there are two populations, with different sizes but, given the completeness limitations, similar masses.

3.5.2 The Core Mass Distribution

Figure 3.10 shows the differential (dN/dM) core mass distribution (CMD) for the 44 secure detections. These include both starless cores and cores with protostars. The masses are taken from table 3.2, and error bars are \sqrt{N} statistical errors only. The shaded regions on the figure represent the range in detection limit for a point source (left), and the 50% completeness limit for sources with a FWHM of 70'' (right), which is approximately the average FWHM of the sample. We do not attempt to correct for incompleteness in the mass function. Most sources are found in the higher noise regions of the map; therefore the mass function is likely to be incomplete below 0.5

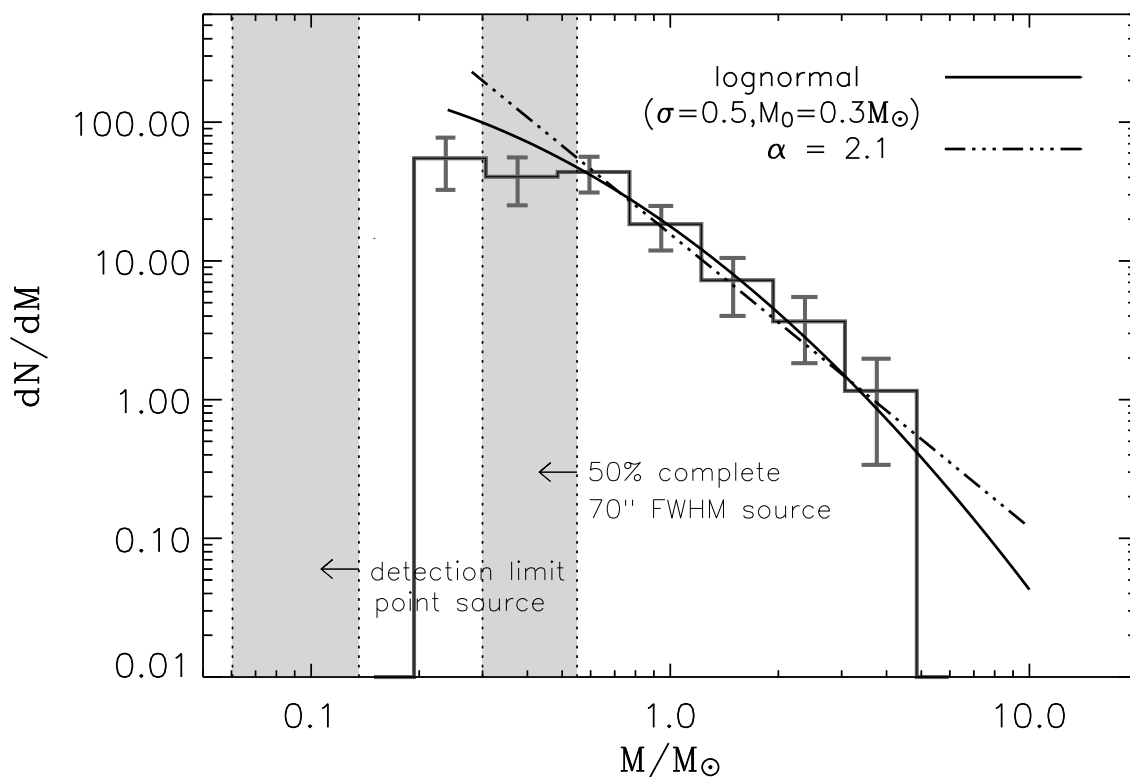
M_{\odot} .

Figure 3.10 Differential mass distribution of all detected sources for masses calculated with $T_D = 10$ K. The range in completeness, due to the range in local rms, is indicated by the shaded regions. To the left is the range in detection limit for a point source, and to the right is the range in 50% completeness limit for $70''$ FWHM sources, which is similar to the average source size of the sample. The best fitting power law ($\alpha = 2.1$) is shown, as well as the best-fitting lognormal function.

The CMD above $0.5 M_{\odot}$ can be fitted with either a power law ($N(M) \propto M^{-\alpha}$), for which the best fit is $\alpha = 2.1 \pm 0.3$, or with a lognormal function (equation (2.5)), for which we find $\sigma_M = 0.5 \pm 0.4$ and $M_0 = 0.3 \pm 0.7 M_{\odot}$ (where σ_M is the width of the distribution, and M_0 is the characteristic mass). The power law fit has a reduced chi-squared of $\chi_r^2 = 0.4$, and the lognormal fit $\chi_r^2 = 0.3$. The slightly better χ_r^2 value for the lognormal function reflects the tendency of the distribution to flatten at lower masses, but incompleteness prevents us from distinguishing between these two functions.

The CMD depends on assumptions about distance, opacity, and dust temperature. Experiments in which cores in the main cluster were given higher temperatures, or small cores were given higher temperatures, produced little change in the mass distribution. If cores in the L1688 cluster are assigned $T_D = 20$ K and other cores assigned $T_D = 10$ K, the best-fit value becomes $\alpha = 2.2$ for $M > 0.5 M_\odot$, insignificantly different. However, the evidence for a turnover at low masses became even less significant. Such effects should be considered before inferring turnovers in CMDs.

Johnstone et al. (2000) (see their figure 7) fit the cumulative mass distribution for 850 μm cores within the L1688 region, assuming $T_D = 20$ K, with a broken power law. They found $\alpha_1 = 1.5$ for masses less than about $0.6 M_\odot$ and $\alpha_2 = 2.5$ for $M > 0.6 M_\odot$. The Johnstone et al. (2000) sample is complete down to about $M \sim 0.4 M_\odot$. If we assume $T_D = 20$ K, the best-fit power law slope remains $\alpha = 2.1$, but our completeness limit becomes $0.2 M_\odot$. Thus, our mass function declines less rapidly than that of Johnstone et al. (2000), but the difference is not very significant. Since Johnstone et al. (2000) split some of our sources into multiple, smaller sources, it is not unexpected that they would find a larger value of α . Stanke et al. (2006) do not give a table of masses, but their CMD extends up to roughly $3 M_\odot$, similar to our result, despite differences in source identification and mass calculation. They argue for breaks in their CMD around 0.2 and $0.7 M_\odot$, with $\alpha \sim 2.6$ for large masses. Similarly, Motte et al. (1998) found $\alpha = 2.5$ above $0.5 M_\odot$ for a broken power-law fit to cores in the Ophiuchus cluster. Broken power-law fits tend to produce steeper slopes at higher masses, and the slopes are steeper if a higher break mass is assumed, suggesting that lognormal fits may be appropriate.

The CMD is naturally compared to predictions from models of turbulent fragmentation in molecular clouds. Padoan & Nordlund (2002) argue that turbulent fragmentation naturally produces a power law with $\alpha = 2.3$ (for the differential CMD that we plot). However, Ballesteros-Paredes et al. (2006) question this result, showing that the shape of the CMD depends strongly on Mach number in the turbulence. As the numerical simulations develop further, the observed CMD will provide a powerful observational constraint, with appropriate care in turning the simulations into

observables.

The shape of the CMD may also be related to the process that determines final stellar masses. Assuming the simplest case in which a single process dominates the shape of the stellar initial mass function (IMF), the IMF should closely resemble the original CMD if stellar masses are determined by the initial fragmentation into cores (Adams & Fatuzzo, 1996). Alternatively, if stellar masses are determined by other processes, such as further fragmentation within cores, merging of cores, competitive accretion, or feedback, the IMF need not be related simply to the CMD (e.g., Ballesteros-Paredes et al. 2006).

The IMF itself is still uncertain (Scalo, 2005). For example, the Salpeter IMF would have $\alpha = 2.35$ (Salpeter, 1955) using our conventions, but more recent work on the local IMF finds evidence for a break in the slope around $1 M_{\odot}$. The slope above the break depends on the choice of break mass. For example, Reid, Gizis, & Hawley (2002) find $\alpha = 2.5$ above $0.6 M_{\odot}$, and $\alpha = 2.8$ above $1 M_{\odot}$. Chabrier (2003) suggests $\alpha = 2.7$ ($M > 1 M_{\odot}$), while Schröder & Pagel (2003) finds $\alpha = 2.7$ for $1.1 < M_{\star} < 1.6 M_{\odot}$ and $\alpha = 3.1$ for $1.6 < M_{\star} < 4 M_{\odot}$. Given the uncertainties and the differences between fitting single and broken power laws, all these values for α are probably consistent with each other and with determinations of the CMD.

Currently, we cannot separate prestellar cores from more evolved objects in Ophiuchus, so a direct connection to the IMF is difficult to make. After combining these data with *Spitzer* data it will be possible to determine the evolutionary state of each source and compare the mass function of prestellar cores only (chapter 6).

3.5.3 Clustering

The majority of the sources detected with Bolocam in Ophiuchus are very clustered. Of the 44 sources, 36 are multiple (table 3.2) with a neighboring source within $3'$, corresponding to 22500 AU at a distance of 125 pc. The average separation for the entire sample is $153''$, or 19,000 AU. If we consider only sources in the L1688 region for comparison to previous studies, the mean separation is $116''$, or 14,500 AU. The

median separation in L1688 is substantially smaller ($69'' = 8600$ AU). The median separation in L1688 is very similar to the mean size of the sources in the sample, $68''$. This indicates that many source pairs are barely resolved. It also means that the measured size of many sources is limited to something like the mean separation, since the Gaussian fitting routine takes into account the distance to the nearest neighbor when determining source size.

The median separation of 8600 AU for the L1688 cluster is only slightly larger than the fragmentation scale of 6000 AU suggested by Motte et al. (1998) in their study of the main Ophiuchus cluster by examining the mean separation between cores in their data. Resolution effects likely play a role here, as our resolution (3900 AU) is approximately twice that of Motte et al. (1998). Stanke et al. (2006) find two peaks in the distribution of source separations of neighboring cores (~ 5000 AU and $\sim 13,000$ AU), suggesting that they also distinguish the cores in the Ophiuchus cluster from those in the more extended cloud. The median core separation is still smaller than the median separation of T Tauri stars in Taurus of 50,000 AU (Gomez et al., 1993) as pointed out by Motte et al. (1998).

Another description of source clustering is provided by the two-point correlation function, as was used in chapter 2 and in Johnstone et al. (2000). Figure 3.11 plots $H(r)$, $w(r)$, and $\log(w(r))$ versus the log of the distance between sources, r . $H(r)$ is the fractional number of source pairs with a separation between $\log(r)$ and $\log(r) + d\log(r)$, and is plotted in figure 3.11 (upper panel) for the Ophiuchus sample (solid line), and for a uniform random distribution of sources (dashed lines). Because it is discontinuous from the rest of the map, the northeastern streamer is not included in this analysis.

The top panel of figure 3.11 shows an excess in $H_s(r)$ over the random sample $H_r(r)$ for small separations. The excess indicates that the sources in Ophiuchus are not randomly distributed within the cloud, but clustered on small scales. The middle panel shows that the two-point correlation function for the Ophiuchus data exceeds zero by 2.5σ for $r < 4 \times 10^4$ AU, while the random distribution shows no correlation ($w(r) = 0$). The correlation function can be fit with a power law, ($w(r) \propto r^{-\gamma}$,

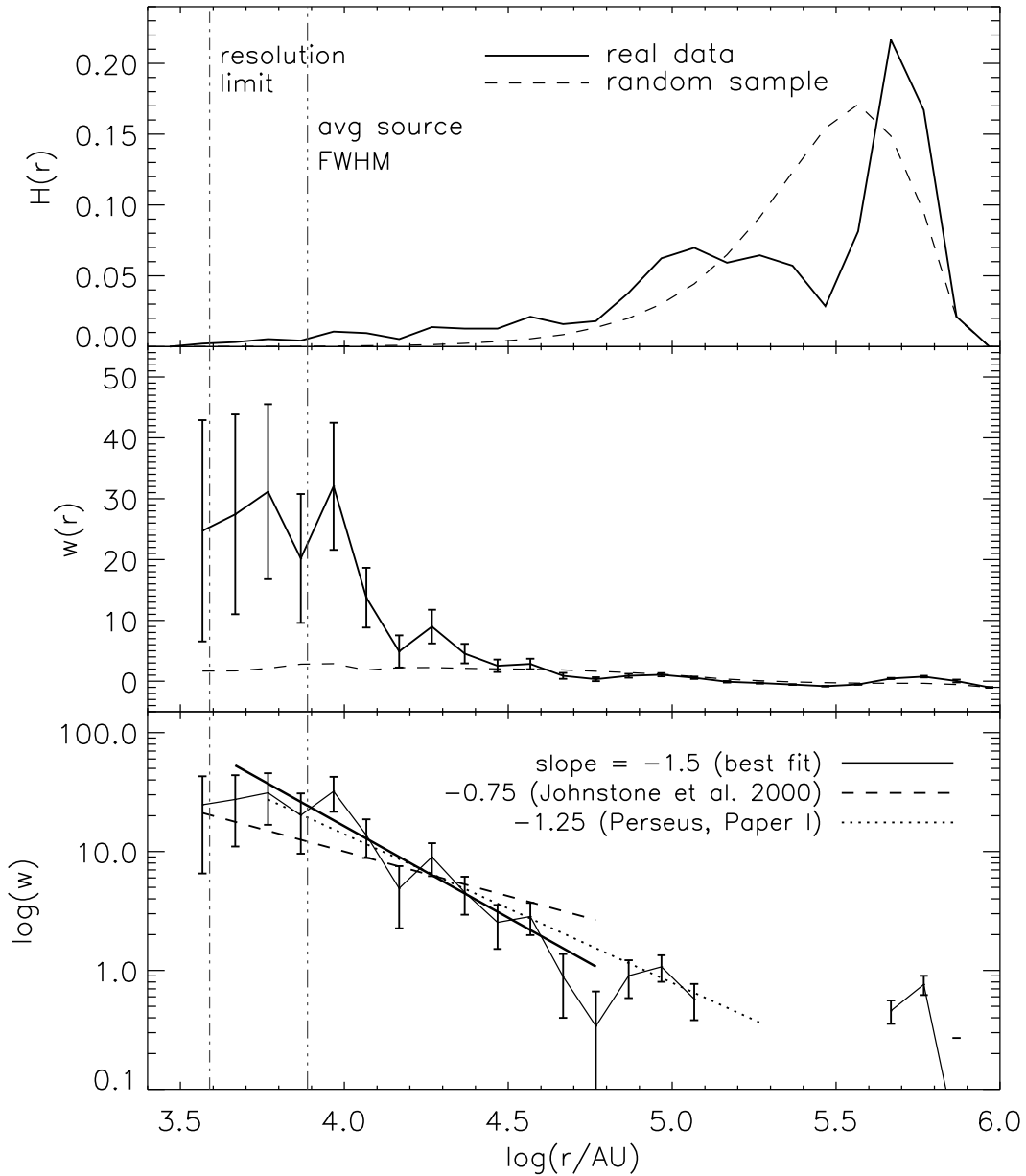


Figure 3.11 Top: $H(r)$, the fractional number of source pairs between $\log(r)$ and $d\log(r)$, versus $\log(r)$. The solid line indicates the real data, and the dashed line is for a uniform random distribution of sources with the same RA/Dec limits as the real sample. In all plots, the resolution limit and the average source FWHM are shown. Middle: Two-point correlation function $w(r)$, with \sqrt{N} errors. Bottom: Log of $w(r)$, with power-law fits. The best fit slope is -1.5 ± 0.3 . The slope found by Johnstone et al. (2000) in Ophiuchus is shallower (-0.75), while the slope found in Perseus in chapter 2 was similar (-1.25 ± 0.06).

bottom panel); the best fit gives $\gamma = 1.5 \pm 0.3$ for $1 \times 10^4 \text{ AU} < r < 4 \times 10^4 \text{ AU}$, with $\chi_r^2 = 1.2$. The correlation function for Perseus (chapter 2) was characterized by $\gamma = 1.25 \pm 0.06$ ($\chi_r^2 = 0.7$) for $2 \times 10^4 \text{ AU} < r < 2 \times 10^5 \text{ AU}$.

Stanke et al. (2006) found $\gamma = 0.63$ out to $r \sim 1 \times 10^5 \text{ AU}$. Johnstone et al. (2000) also fitted the correlation for the Ophiuchus cluster with a shallower power law, $\gamma = 0.75$ for $r < 3 \times 10^4$ in the L1688 cluster region of Ophiuchus. This power law is also shown in figure 3.11, but it clearly does not fit our data. Johnstone et al. (2000) were able to measure the correlation function to smaller scales, $r = 4.5 \times 10^3 \text{ AU}$, than this study, which may result in some discrepancy in the best-fit power law between the two data sets. The correlation function does appear flatter at smaller separations, but the slope there may be complicated by blending. If the correlation function is restricted to sources in the L1688 cluster, the slope becomes more consistent with those found by Johnstone et al. (2000) and Stanke et al. (2006).

We conclude from this analysis that the sources in Ophiuchus are clearly clustered. Determining the parameters of the correlation function is complicated by effects of map size and resolution.

3.5.4 Extinction threshold

Johnstone et al. (2004) suggested that there is a threshold at $A_V = 15 \text{ mag}$ in Ophiuchus for the formation of cores, with 94% of the mass in cores found at or above that extinction level. They did see cores below that level, but they were faint (low peak flux) and low in mass. Johnstone et al. (2004) mapped 4 deg^2 of Ophiuchus at $850 \mu\text{m}$ and compared their data to an extinction map of Ophiuchus created from 2MASS and R-band data as part of the COMPLETE project. Comparison of our own extinction map (figure 3.6) with the COMPLETE extinction map shows reasonable agreement, so we use our extinction map.

We use a simple analysis (see §2.5.4) to study the extinction threshold. Figure 3.12 plots the probability of finding a 1.1 mm core in Ophiuchus as a function of A_V , where the probability is calculated from the extinction map as the number of $50''$

pixels containing a 1.1 mm core divided by the total number of pixels at a given A_V . Error bars are Poisson statistical errors.

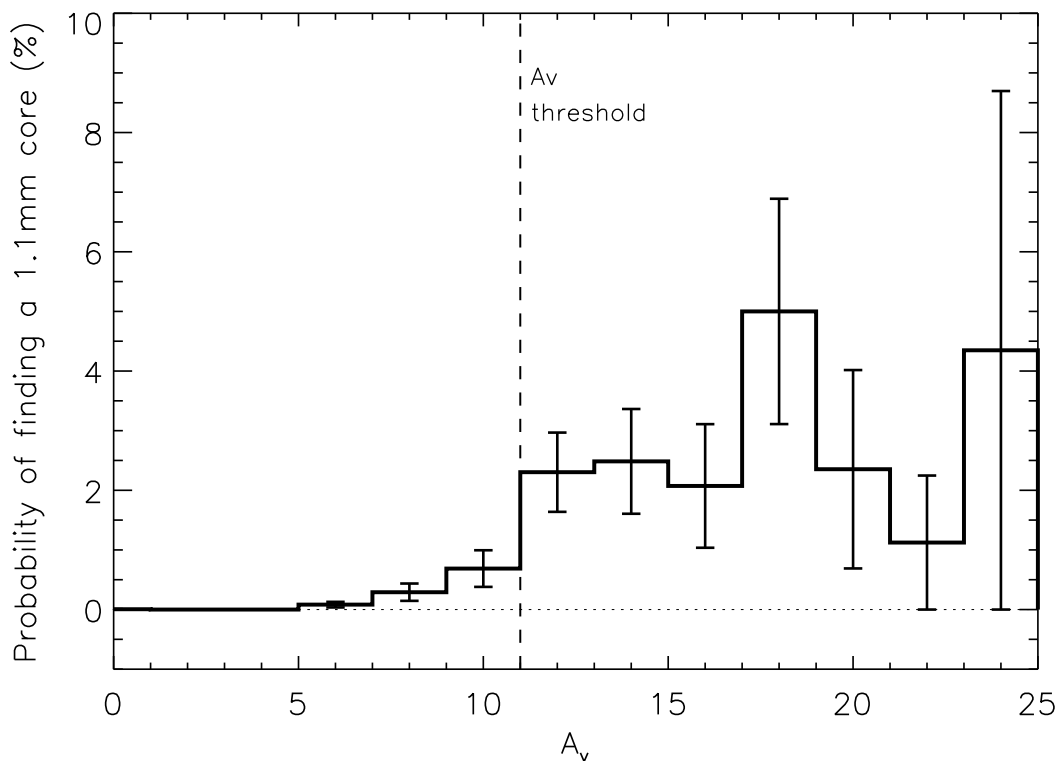


Figure 3.12 Probability of finding a 1.1 mm core as a function of A_V . The probability is the number of $50''$ pixels at a given A_V containing one or more 1.1 mm cores, divided by the total number of pixels at that A_V . Error bars are Poisson statistical errors. The dashed vertical line shows our proposed threshold at $A_V = 11$ mag.

Very few sources are found below $A_V = 11$ mag, and 88% of the mass in cores is found above $A_V = 10$ mag (see table 3.3). We suggest, therefore, that $A_V = 11$ mag is the extinction limit for finding 1.1 mm cores in Ophiuchus. The probability of finding a core increases with A_V beyond this point, although the uncertainties are large at high A_V because there are few pixels in the extinction map at very high extinctions. This extinction limit is much higher than that found for Perseus in chapter 2 ($A_V = 5$ mag).

To explore this issue further, we plot in figure 3.13 source total flux density, peak flux density, FWHM, and mass versus A_V . All bright (peak > 0.5 Jy) and massive

($M > 1.5M_{\odot}$) cores are found above the extinction threshold of $A_V = 11$ mag. Note, however, that the tentative detections listed in table 3.1 are in regions with $A_V < 10$ mag. In contrast to the Johnstone et al. (2004) study, we find many (12 out of the total core sample of 44) bright (total flux density > 3 Jy) and massive ($M > 2M_{\odot}$) sources at $A_V < 15$ mag. Thus conclusions about thresholds likely depend on sensitivity to large structures, slight differences in extinction contours, and differing resolution.

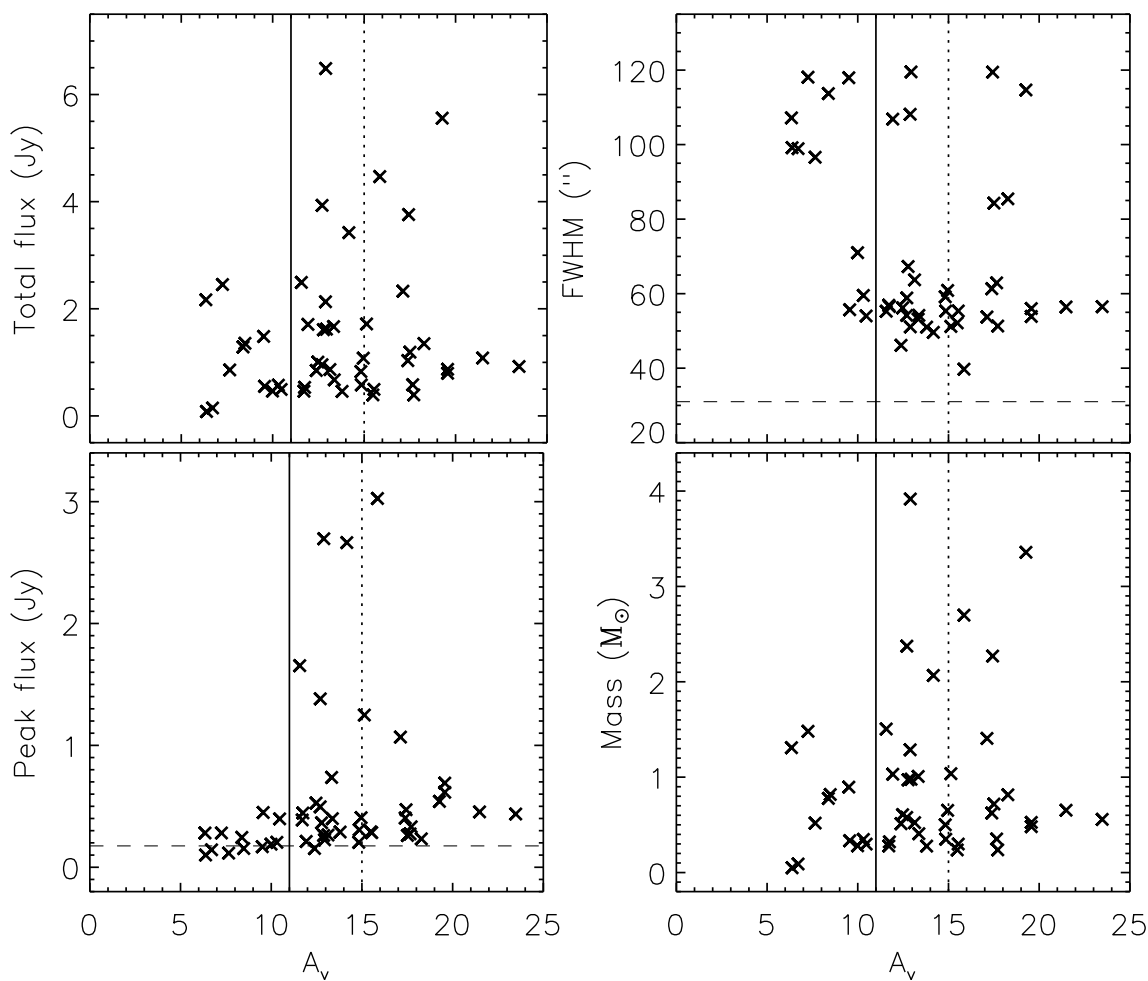


Figure 3.13 1.1 mm source properties versus A_V . The dotted vertical lines are the $A_V = 15$ mag threshold proposed by Johnstone et al. (2004). The solid vertical line is the $A_V = 11$ mag extinction threshold derived from figure 3.12. The dashed horizontal lines are the beam size in the upper right panel and the average 4σ detection limit in the lower left panel.

Table 3.3. Cumulative mass as a function of extinction for sources in Ophiuchus

Min. A_V mag	Area (%)	Cloud Mass (M_\odot)	Percent (%)	Core Mass (M_\odot)	Percent (%)	Mass Ratio ¹ (%)
2	100	2300	100	42	100	1.8
4	39	1500	65	42	100	2.8
6	17	920	40	42	100	4.6
8	8.8	640	28	39	93	6.1
10	5.5	470	20	37	88	7.9
12	3.8	350	15	33	79	9.4
14	2.3	240	10	20	47	8.3
16	1.4	170	7.4	12	29	7.1
18	0.9	120	5.2	6.4	15	5.3
20	0.5	73	3.1	1.2	2.9	1.6

Note. — Cloud areas and masses are calculated from the extinction and conversions from §3.4.2.3. Core masses are taken from table 3.2.

¹The Mass Ratio is computed from the ratio of core mass to cloud mass within the same contour of A_V .

Cloud areas and masses within a given A_V contour, measured from the extinction map, are listed in table 3.3 along with total core masses within the same A_V contour. The percentages of the total cloud and core masses are also given. Finally, the mass ratio, or fraction of the cloud mass that is contained in dense cores is listed in the last column. This is similar to table 2 of Johnstone et al. (2004), except that our cloud and core masses are cumulative and we use bins of $A_V = 2$ mag. Even with our lower threshold, nearly half the total core mass lies above the $A_V = 14$ mag contour, which occupies only 2.3% of the cloud area and 10% of the cloud mass. Dense cores are clearly concentrated in the regions of high extinction; the ratio of core to cloud mass increases from about 2% at the lowest contour ($A_V = 2$) to an average of 7.4% for contours between 8 and 18 mag. (The contour above 20 mag has such little area that the core mass fraction is not very reliable.)

3.6 Summary

We present a 1.1 mm dust continuum emission map of 10.8 deg² of the Ophiuchus molecular cloud. We detected 44 sources at 4σ or greater, almost all concentrated around well known clusters (near the dark clouds L1688, L1689, and L1709). A few weaker sources (3σ) were seen along the eastern streamer of the cloud, coincident with a filament seen in both extinction (figure 3.6) and emission at 160 μm (figure 3.5). These cores have been previously seen in maps of CO, but ours are the first millimeter dust continuum observations of the eastern streamer. We did not detect any emission in the northeastern streamer, and in fact most of the cloud area has no detectable sources.

Visually, the 4σ sources appear highly clustered, and this impression is confirmed by the two-point correlation function, the fraction of multiple sources, and the median separation. Fully 82% of the sources are classified as multiple (i.e., another source lies within $3'$).

Most sources are round as measured at the FWHM, but many are elongated when measured at lower contour levels. We suggest that this difference is reflective of the fact that many cores are relatively spherical condensations within more elongated filaments. Filamentary structure with embedded condensations is the dominant morphological theme.

The total mass of the 1.1 mm sources is only $42 M_{\odot}$, approximately 0.4% to 1.8% of the total cloud mass and lower than in Perseus (chapter 2), while the total mass in 1.1 mm emission above 4σ is $79 M_{\odot}$. The differential core mass distribution (CMD) can be fitted with a power law with slope $\alpha = -2.1 \pm 0.3$ or with a lognormal function ($\sigma_M = 0.5 \pm 0.4$, $M_0 = 0.3 \pm 0.7 M_{\odot}$). The CMD is similar to that in Perseus, but does not extend as high in mass, with the most massive core containing only $3.9 M_{\odot}$. Core mean densities are quite high, averaging $1.6 \times 10^6 \text{ cm}^{-3}$, implying a short free-fall time.

We suggest an extinction threshold for finding millimeter continuum sources at $A_V = 11$ mag, higher than in Perseus but lower than found in previous studies of

Ophiuchus by Johnstone et al. (2004). Approximately half the total mass of dense cores are in contours of extinction below $A_V = 14$ mag, which was the threshold seen by Johnstone et al. (2004). Still, the cores are clearly concentrated in a small fraction of the cloud area and mass, and in regions of relatively high extinction.

Analysis of these data in combination with the c2d *Spitzer* maps of Ophiuchus will give a more complete picture of star formation in the cloud (see chapter 6).

Acknowledgments

We would like to thank A. Urban for assistance observing at the CSO, and other members of the larger Bolocam team for instrumental support, including A. Goldin, A. Lange, P. Maloney, and P. Rossinot. We thank the Lorentz Center in Leiden for hosting several meetings that contributed to this work. Support for this work, part of the *Spitzer* Legacy Science Program, was provided by NASA through contracts 1224608 and 1230782 issued by the Jet Propulsion Laboratory, California Institute of Technology, under NASA contract 1407. Bolocam was built and commissioned under grants NSF/AST-9618798 and NSF/AST-0098737. KEY and GL were supported by NASA under Grants NGT5-50401 and NGT5-50384, respectively, issued through the Office of Space Science. Additional support came from NASA Origins grant NNG04GG24G to NJE and NSF grant AST 02-06158 to JG. MLE acknowledges support of an NSF Graduate Research Fellowship. SG was supported in part by a Millikan fellowship at Caltech and CSO grant NSF/AST-9980846.

Bibliography

- Adams, F. C., & Fatuzzo, M. 1996, *ApJ*, 464, 256
- Allen, L. E., Myers, P. C., DiFrancesco, J., Matheiu, R., Chen, H., & Young, E. 2002, *ApJ*, 566, 993
- Ballesteros-Paredes, J., Gazol, A., Kim, J., Klessen, R. S., Jappsen, A.-K., & Tejero, E. 2006, *ApJ*, 637, 384
- Bohlin, R. C., Savage, B. D., & Drake, J. F. 1978, *ApJ*, 224, 132
- Cambr esy, L. 1999, *A&A*, 345, 965
- Castelaz, M. W., Gehrz, R. D., Grasdalen, G. L., & Hackwell, J. A. 1985, *PASP*, 97, 924
- Chabrier, G. 2003, *PASP*, 115, 763
- de Geus, E. J., de Zeeuw, P. T., Lub, J. 1989, *A&A*, 216, 44
- Enoch, M. L., Glenn, J., Evans, N. J., II, Sargent, A. I., Young, K. E., & Huard, T. L. 2007, *ApJ*, in press
- Enoch, M. L., Young, K. E., Glenn, J., Evans, N. J., II, Golwala, S., Sargent, A. I., Harvey, P., et al. 2006, *ApJ*, 638, 293 (Paper I)
- Evans, N. J., II, Allen, L. E., Blake, G. A., Boogert, A. C. A., Bourke, T., Harvey, P. M., Kessler, J. E., et al. 2003, *PASP*, 115, 965
- Gomez, M., Hartmann, L., Kenyon, S. J., & Hewett, R. 1993, *AJ*, 105, 1927
- Goodman, A. A., 2004, in *Star Formation in the Interstellar Medium*, ASPC, 323, 171 (<http://cfa-www.harvard.edu/COMPLETE>)
- Huard, T. L., Myers, P. C., Murphy, D. C., Crews, L. J., Lada, C. J., Bourke, T. L., Crapsi, A., Evans, N. J., II, McCarthy, D. W., Jr., & Kulesa, C. 2006, *ApJ*, 640, 391

- Imanishi, K., Koyama, K., & Tsuboi, Y. 2001, *ApJ*, 557, 747
- Johnstone, D., Di Francesco, J., & Kirk, H. 2004, *ApJ*, 611, L45
- Johnstone, D., Wilson, C. D., Moriarty-Schieven, G., Joncas, G., Smith, G., Gregersen, E., & Fich, M. 2000, *ApJ*, 545, 327
- Lada, C. J., Alves, J., & Lada, E. A. 1999, in *The Physics and Chemistry of the Interstellar Medium*, editors V. Ossenkopf, J. Stutzki, G. Winnewisser, 161
- Leous, J. A., Feigelson, E. D., Andre, P., & Montmerle, T. 1991, *ApJ*, 379, 683
- Loren, R. B. 1989, *ApJ*, 338, 902
- Mezger, P. G., Sievers, A., Zylka, R., Haslam, C. G. T., Kreysa, E., & Lemke, R. 1992, *A&A*, 265, 743
- Motte, F., André, P., & Neri, R. 1998, *A&A*, 336, 150
- Padoan, P., & Nordlund, Å. 2002, *ApJ*, 576, 870
- Reid, I. N., Gizis, J. E., & Hawley, S. L. 2002, *AJ*, 124, 2721
- Ridge, N. A., Di Francesco, J., Kirk, H., Li, D., Goodman, A. A., Alves, J. F., Arce, H. G., et al. 2006, *ApJ*, 131, 2921
- Rieke, G. H., & Lebofsky, M. J. 1985, *ApJ*, 288, 618
- Salpeter, E. E. 1955, *ApJ*, 121, 161
- Sandell, G. 1994, *MNRAS*, 271, 75
- Scalo, J., 2005 in *The Stellar Initial Mass Function Fifty Years Later*, Kluwer Academic Publishers, editors E. Corbelli, F. Palla, and H. Zinnecker, p. 23
- Schröder, K.-P., & Pagel, B. E. J. 2003, *MNRAS*, 343, 1231
- Stanke, T., Smith, M. D., Gredel, R., & Khanzadyan, T. 2006, *A&A*447, 609

Tachihara, K., Mizuno, A., & Fukui, Y. 2000, ApJ, 528, 817

Visser, A. E., Richer, J. S., & Chandler, C. J. 2002, AJ, 124, 2756

Weintraub, D. A., Kastner, J. H., Griffith, L. L., & Campins, H. 1993, AJ, 105, 271

Wilking, B. A., Lada, C. J., & Young, E. T. 1989, ApJ, 340, 823

Wilking, B. A., Meyer, M. R., Robinson, J. G., & Greene, T. P. 2005, AJ, 130, 1733